Computational Methods for Transition States and Pathways in Rare Events

Edited by Shuting Gu

First published 2025

ISBN: 978-1-032-99647-9 (hbk)
ISBN: 978-1-032-99718-6 (pbk)
ISBN: 978-1-003-60565-2 (ebk)

Chapter 4

Enhanced Numerical Schemes in IMF for Transition States

DOI: 10.1201/9781003605652-4

The funder for this chapter is The Natural Science Foundation of Top Talent of SZTU GDRC202137, the National Natural Science Foundation of China (NSFC) 11901211 and Shenzhen Technology University

CRC Press
Taylor & Francis Group
Boca Raton London New York

CRC Press is an imprint of the
Taylor & Francis Group, an **informa** business

Enhanced Numerical Schemes in IMF for Transition States

As discussed in section 2.3, the Iterative Minimization Formulation (IMF) identifies the saddle points by solving a sequence of minimization subproblems. These involve a position variable and an orientation vector, each optimized independently. This chapter focuses exclusively on minimizing the position variable-referred to as the translation step. We reformulate this minimization problem into a gradient flow dynamics framework and employ advanced numerical techniques to solve it efficiently. Specifically, the convex splitting method and the scalar auxiliary variable (SAV) approach are employed in sections 4.1 and 4.2, respectively, to locate transition states. These strategies allow for larger time step sizes, significantly enhancing computational efficiency.

Moreover, recognizing the challenges in calculating saddle points in the H^{-1} metric compared to the L^2 metric, we introduce a projection-based adaptation to the IMF in section 4.3. This method incorporates a straightforward linear projection operator into the L^2 metric dynamics, enabling the efficient computation of transition states in the H^{-1} metric while substantially reducing computational costs.

Given that the IMF relies heavily on the quality of initial conditions and exhibits only local convergence, we propose an innovative enhancement in section 4.4. By incorporating a proximal function as a penalty term into the auxiliary function, We ensure strict convexity of the subproblems. This development leads to the iterative proximal minimization (IPM) method, which guarantees the existence of a well-defined minimizer for each subproblem, regardless of the initial conditions. Notably, this method demonstrates rapid convergence even when the initial estimate is far from the true saddle point.

DOI: 10.1201/9781003605652-4

Let $\mathcal{M}$ denote a function space over the interval $[a, b]$, such as the Hilbert space $H^1([a, b])$ or a subspace of $L^2([a, b])$. For higher-dimensional cases, the same principles apply. Our goal is to identify the transition state of the energy functional F on $\mathcal{M}$.

Assume that the second-order variational derivative (Hessian) of F in $\mathcal{M}$, denoted as $\mathbf{H}(\phi) := \delta_\phi^2 F(\phi)$, exists. The IMF described in section 2.3 can then be reformulated as:

$$\begin{cases} v^{(k+1)} = \underset{\|v\|=1}{\operatorname{argmin}} \left\langle v, \mathbf{H}(\phi^{(k)})v \right\rangle, & \text{(4.1a)} \\ \phi^{(k+1)} = \underset{\phi}{\operatorname{argmin}}\, L(\phi; \phi^{(k)}, v^{(k+1)}), & \text{(4.1b)} \end{cases}$$

where the auxiliary functional L is defined as:

$$L(\phi; \phi^{(k)}, v^{(k+1)}) = (1-\alpha)F(\phi) + \alpha F(\phi - \tilde{\phi}) - \beta F(\phi^{(k)} + \tilde{\phi}), \tag{4.2}$$

with $\tilde{\phi}$ given by:

$$\tilde{\phi} := (v^{(k+1)} \otimes v^{(k+1)})(\phi - \phi^{(k)}). \tag{4.3}$$

Here, $v^{(k+1)}$ belongs to the tangent space of $\mathcal{M}$, denoted as $\mathcal{T}_\mathcal{M}$. The operation $(u \otimes v)\phi = \langle v, \phi \rangle\, u$ is defined for $u, v \in \mathcal{T}_\mathcal{M}$.

The solution of the variational subproblem (4.1b) at the k-th IMF cycle is approximated by the steady state of the gradient flow associated with L under the chosen metric:

$$\frac{\partial \phi}{\partial t} = -\frac{\delta L}{\delta \phi}, \quad \text{in } L^2 \text{ metric}, \tag{4.4}$$

or

$$\frac{\partial \phi}{\partial t} = \Delta \frac{\delta L}{\delta \phi}(\phi), \quad \text{in } H^{-1} \text{ metric}. \tag{4.5}$$

It is important to note that in the H^{-1} metric, the inner product used in the rotation step remains identical so that in the L^2 metric:

$$\left\langle v, -\Delta \mathbf{H}(\phi^{(k)})v \right\rangle_{H^{-1}} = \left\langle v, \mathbf{H}(\phi^{(k)})v \right\rangle_{L^2}.$$

In subsequent sections, we introduce the convex splitting method for the IMF applied to (4.4), and the SAV method to (4.5). Notably, both methods can be applied to interchangeably to these equations with effective results.

4.1 CONVEX SPLITTING METHOD IN IMF

Suppose the energy functional $F(\phi)$ can be decomposed using a convex splitting form:

$$F(\phi) = F_c(\phi) - F_e(\phi), \tag{4.6}$$

where $F_c(\phi)$ and $F_e(\phi)$ are both convex with respect to ϕ. Substituting (4.6) into the auxiliary functional L defined in (4.2), we derive its convex splitting form:

$$L(\phi;\, \phi^{(k)}, v^{(k+1)}) = L_c(\phi;\, \phi^{(k)}, v^{(k+1)}) - L_e(\phi;\, \phi^{(k)}, v^{(k+1)}), \tag{4.7}$$

where the components L_c and L_e are given by:

$$L_c(\phi; \phi^{(k)}, v^{(k+1)}) = \begin{cases} F_c(\phi) + \alpha F_e(\phi) + \alpha F_c(\phi - \tilde{\phi}) + \beta F_e(\phi^{(k)} + \tilde{\phi}), \text{if } \alpha \geq 0, \beta \geq 0; \\ F_c(\phi) + \alpha F_e(\phi) + \alpha F_c(\phi - \tilde{\phi}) - \beta F_c(\phi^{(k)} + \tilde{\phi}), \text{if } \alpha \geq 0, \beta \leq 0; \\ F_c(\phi) - \alpha F_c(\phi) - \alpha F_e(\phi - \tilde{\phi}) + \beta F_e(\phi^{(k)} + \tilde{\phi}), \text{if } \alpha \leq 0, \beta \geq 0, \end{cases} \tag{4.8}$$

and

$$L_e(\phi; \phi^{(k)}, v^{(k+1)}) = \begin{cases} F_e(\phi) + \alpha F_c(\phi) + \alpha F_e(\phi - \tilde{\phi}) + \beta F_c(\phi^{(k)} + \tilde{\phi}), \text{if } \alpha \geq 0, \beta \geq 0; \\ F_e(\phi) + \alpha F_c(\phi) + \alpha F_e(\phi - \tilde{\phi}) - \beta F_e(\phi^{(k)} + \tilde{\phi}), \text{if } \alpha \geq 0, \beta \leq 0; \\ F_e(\phi) - \alpha F_e(\phi) - \alpha F_c(\phi - \tilde{\phi}) + \beta F_c(\phi^{(k)} + \tilde{\phi}), \text{if } \alpha \leq 0, \beta \geq 0. \end{cases} \tag{4.9}$$

Property 4.1 *The terms $L_c(\phi;\, \phi^{(k)}, v^{(k+1)})$ and $L_e(\phi;\, \phi^{(k)}, v^{(k+1)})$ are convex with respect to ϕ for any given $\phi^{(k)}$ and any $v^{(k+1)}$.*

Proof Property 4.1 *We demonstrate the convexity of L_c in this specific case: $\alpha \geq 0, \beta \geq 0$. The convexity of L_e and the other cases follow similarly.*

It suffices to show that the terms $F_c(\phi - \tilde{\phi})$ and $F_e(\phi^{(k)} + \tilde{\phi})$ in (4.8) are convex with respect to ϕ. Let H_c and H_e represent the Hessian matrices of $F_c(\phi)$ and $F_e(\phi)$, respectively. By definition, both are semi-positive definite due to the convexity of F_c and F_e.

Using the definition of $\tilde{\phi}$ in (4.3), the second-order variational derivatives of $F_c(\phi - \tilde{\phi})$ and $F_e(\phi^{(k)} + \tilde{\phi})$ are:

$$[I - (v \otimes v)] H_c(\phi - \tilde{\phi}) [I - (v \otimes v)]$$

and

$$(v \otimes v) H_e(\phi^{(k)} + \tilde{\phi})(v \otimes v),$$

respectively, where $v = v^{(k+1)}$. Since $v \neq 0$, these projected Hessian matrices remain semi-positive definite, completing the proof.

For simplicity, we focus on the case $\alpha \geq 0$ and $\beta \geq 0$, omitting $\phi^{(k)}$ and $v^{(k+1)}$ from the notation of $L(\phi, \phi^{(k)}, v^{(k+1)})$, $L_c(\phi, \phi^{(k)}, v^{(k+1)})$ and $L_e(\phi, \phi^{(k)}, v^{(k+1)})$. Let ϕ^n denote the numerical solution at the time level t_n. The time-discrete scheme for the gradient flow (4.4), based on the convex splitting method, is given by:

$$\frac{\phi^{n+1} - \phi^n}{\Delta t} = -\left[\frac{\delta L_c}{\delta \phi}(\phi^{n+1}) - \frac{\delta L_e}{\delta \phi}(\phi^n) \right], \tag{4.10}$$

where

$$\begin{aligned}\frac{\delta L_c}{\delta\phi}(\phi) = \frac{\delta F_c}{\delta\phi}(\phi) + \alpha\frac{\delta F_e}{\delta\phi}(\phi) \\ + \alpha\Big(I - (v^{(k+1)}\otimes v^{(k+1)})\Big)\frac{\delta F_c}{\delta\phi}\left(\phi - (v^{(k+1)}\otimes v^{(k+1)})(\phi-\phi^{(k)})\right) \\ + \beta(v^{(k+1)}\otimes v^{(k+1)})\frac{\delta F_e}{\delta\phi}\left(\phi^{(k)} + (v^{(k+1)}\otimes v^{(k+1)})(\phi-\phi^{(k)})\right),\end{aligned}$$

and $\frac{\delta L_e}{\delta\phi}(\phi)$ is obtained similarly by swapping the indices "c" and "e." The initial condition is $\phi^0 = \phi^{(k)}$.

Lemma 4.1 *Suppose that $\phi,\ \psi : [0,1]\times\mathbb{R}^+ \to \mathbb{R}$ are two periodic functions, and $L(\phi)$ in (4.2) has the convex splitting form $L(\phi) = L_c(\phi) - L_e(\phi)$ as defined in (4.7). Then the following inequality holds:*

$$L(\phi) - L(\psi) \le \langle \delta_\phi L_c(\phi) - \delta_\phi L_e(\psi), \phi - \psi\rangle_{L^2},$$

where $\delta_\phi L_c$ and $\delta_\phi L_e$ denote the first-order variational derivatives of L_c and L_e with respect to ϕ, respectively.

Theorem 4.1 *If the energy functional $F(\phi)$ has the convex splitting form $F = F_c - F_e$, then the time-discrete scheme (4.10) is unconditionally energy stable. Specifically, for any time step size $\Delta t > 0$, the following inequality holds:*

$$L(\phi^{n+1}; \phi^{(k)}, v^{(k+1)}) \le L(\phi^n; \phi^{(k)}, v^{(k+1)}), \quad \forall n \in \mathbf{N},$$

in each k-th cycle for given ϕ^k and $v^{(k+1)}$.

Proof Theorem 4.1 *From the time-discrete scheme (4.10), we have*

$$\phi^{n+1} - \phi^n = -\Delta t\,\mu^{n+1},$$

where

$$\mu^{n+1} = \delta_\phi L_c(\phi^{n+1}) - \delta_\phi L_e(\phi^n).$$

Substitute $\phi = \phi^{n+1}$ and $\psi = \phi^n$ into Lemma 4.1, we have:

$$\begin{aligned}L(\phi^{n+1}) - L(\phi^n) &\le \langle \delta_\phi L_c(\phi^{n+1}) - \delta_\phi L_e(\phi^n),\ \phi^{n+1} - \phi^n\rangle_{L^2} \\ &= \langle \mu^{n+1}, -\Delta t\,\mu^{n+1}\rangle_{L^2} \\ &= -\Delta t\|\mu^{n+1}\|_{L^2}^2 \\ &\le 0, \quad \forall n \in \mathbf{N}.\end{aligned}$$

This completes the proof.

Linear and unconditional energy-stable schemes

In many cases, the convex splitting form of an energy functional is not unique. Suppose the energy functional $F(\phi)$ admits two convex splitting forms with the following properties:

$$F(\phi) = F_c^{\mathrm{l}}(\phi) - F_e^{\mathrm{n}}(\phi), \tag{4.11}$$

and

$$F(\phi) = \widetilde{F}_c^{\mathrm{n}}(\phi) - \widetilde{F}_e^{\mathrm{l}}(\phi), \tag{4.12}$$

where the superscripts "l" and "n" indicate that the first-order variational derivatives with respect to ϕ"linear" or "nonlinear," respectively. Based on these splitting forms, two convex splitting schemes can be constructed to solve the gradient flow $\partial_t \phi = -\delta_\phi F$:

$$\frac{\phi^{n+1} - \phi^n}{\Delta t} = -\frac{\delta F_c^{\mathrm{l}}}{\delta \phi}(\phi^{n+1}) + \frac{\delta F_e^{\mathrm{n}}}{\delta \phi}(\phi^n), \tag{4.13}$$

and

$$\frac{\phi^{n+1} - \phi^n}{\Delta t} = -\frac{\delta \widetilde{F}_c^{\mathrm{n}}}{\delta \phi}(\phi^{n+1}) + \frac{\delta \widetilde{F}_e^{\mathrm{l}}}{\delta \phi}(\phi^n). \tag{4.14}$$

Both schemes satisfy the unconditional energy stability. However, they differ in the nonlinear terms are treated: Scheme (4.13) is time-explicit for the nonlinear term, while scheme (4.14) is time-implicit for the nonlinear term.

In the context of the IMF, since both F_c and F_e appear in L_c and L_e, adopting a single convex splitting form – (4.11) or (4.12) – inevitably leads to a nonlinear system. To avoid this, we combine both splitting forms and apply them to $L(\phi)$ as defined in (4.2). Specifically, for $\alpha, \beta \geq 0$, we decompose $L(\phi)$ as follows:

$$\begin{aligned}
L(\phi) = \; & F_c^{\mathrm{l}}(\phi) - F_e^{\mathrm{n}}(\phi) - \alpha\Big[\widetilde{F}_c^{\mathrm{n}}(\phi) - \widetilde{F}_e^{\mathrm{l}}(\phi)\Big] \\
& + \alpha\Big[F_c^{\mathrm{l}}(\phi - \tilde{\phi}) - F_e^{\mathrm{n}}(\phi - \tilde{\phi})\Big] - \beta\Big[\widetilde{F}_c^{\mathrm{n}}(\phi^{(k)} + \tilde{\phi}) - \widetilde{F}_e^{\mathrm{l}}(\phi^{(k)} + \tilde{\phi})\Big] \\
= \; & \Big[F_c^{\mathrm{l}}(\phi) + \alpha\widetilde{F}_e^{\mathrm{l}}(\phi) + \alpha F_c^{\mathrm{l}}(\phi - \tilde{\phi}) + \beta\widetilde{F}_e^{\mathrm{l}}(\phi^{(k)} + \tilde{\phi})\Big] \\
& - \Big[F_e^{\mathrm{n}}(\phi) + \alpha\widetilde{F}_c^{\mathrm{n}}(\phi) + \alpha F_e^{\mathrm{n}}(\phi - \tilde{\phi}) + \beta\widetilde{F}_c^{\mathrm{n}}(\phi^{(k)} + \tilde{\phi})\Big] \\
=: \; & L_c(\phi) - L_e(\phi),
\end{aligned}$$

where $\tilde{\phi} = (v^{(k+1)} \otimes v^{(k+1)})(\phi - \phi^{(k)})$. It is straightforward to verify that L_c and L_e are both convex with respect to ϕ.

Using this decomposition, the semi-discrete scheme for (4.4) becomes:

$$\frac{\phi^{n+1} - \phi^n}{\Delta t} = -\left[\frac{\delta L_c}{\delta \phi}\right]^{n+1} + \left[\frac{\delta L_e}{\delta \phi}\right]^{n}, \tag{4.15}$$

where

$$\begin{aligned}\left[\frac{\delta L_c}{\delta\phi}\right]^{n+1} &= \frac{\delta F_c^{\mathrm{l}}}{\delta\phi}(\phi^{n+1}) + \alpha\frac{\delta \widetilde{F}_e^{\mathrm{l}}}{\delta\phi}(\phi^{n+1}) \\ &\quad + \beta(v^{(k+1)}\otimes v^{(k+1)})\frac{\delta \widetilde{F}_e^{\mathrm{l}}}{\delta\phi}\left(\phi^{(k)} + (v^{(k+1)}\otimes v^{(k+1)})(\phi^{n+1}-\phi^{(k)})\right) \\ &\quad + \alpha(I-(v^{(k+1)}\otimes v^{(k+1)}))\frac{\delta F_c^{\mathrm{l}}}{\delta\phi}\left(\phi^{n+1} - (v^{(k+1)}\otimes v^{(k+1)})(\phi^{n+1}-\phi_k)\right),\end{aligned}$$

and

$$\begin{aligned}\left[\frac{\delta L_e}{\delta\phi}\right]^{n} &= \frac{\delta F_e^{\mathrm{n}}}{\delta\phi}(\phi^{n}) + \alpha\frac{\delta \widetilde{F}_c^{\mathrm{n}}}{\delta\phi}(\phi^{n}) \\ &\quad + \beta(v^{(k+1)}\otimes v^{(k+1)})\frac{\delta \widetilde{F}_c^{\mathrm{n}}}{\delta\phi}\left(\phi^{(k)} + (v^{(k+1)}\otimes v^{(k+1)})(\phi^{n}-\phi^{(k)})\right) \\ &\quad + \alpha(I-(v^{(k+1)}\otimes v^{(k+1)}))\frac{\delta F_e^{\mathrm{n}}}{\delta\phi}\left(\phi^{n} - (v^{(k+1)}\otimes v^{(k+1)})(\phi^{n}-\phi^{(k)})\right).\end{aligned}$$

Here, $\phi^0 = \phi^{(k)}$. This scheme is linear and unconditionally energy stable under the given decomposition.

Remark 4.1 *1. When constructing the two convex splitting forms* (4.11) *and* (4.12)*, global convexity across the entire configuration space is not required. For many energy functionals, achieving global convexity for all four components in* (4.11) *and* (4.12) *is infeasible. Instead, convexity needs to hold only locally within a specific range of* ϕ*.*

4.2 SCALAR AUXILIARY VARIABLE METHOD IN IMF

In this section, we apply the scalar auxiliary variable (SAV) method to discretize the gradient flow of $L(\phi)$ within the H^{-1} metric. The SAV framework facilitates the construction of energy-stable numerical schemes for the gradient flow equation (4.5).

The H^{-1} metric inherently conserves mass, with the initial mass given as:

$$m = \int_\Omega \phi(\mathbf{x}, 0)\mathrm{d}\mathbf{x}.$$

To adopt the SAV method, we assume the free energy $F(\phi)$ can be expressed as:

$$F(\phi) = \tfrac{1}{2}\langle\phi, \mathcal{L}\phi\rangle + F_n(\phi),$$

where $\mathcal{L}$ is a symmetric, nonnegative linear operator, and $F_n(\phi)$ is nonlinear component. Furthermore, let $F(\phi)$ and $F_n(\phi)$ be bounded within $[-\widehat{C}_0, \widehat{C}_1]$ and $[-\widetilde{C}_0, \widetilde{C}_1]$, respectively, where $\widehat{C}_0$, $\widehat{C}_1$, $\widetilde{C}_0$, $\widetilde{C}_1 > 0$. By defining $C_0 = \max\{\widehat{C}_0, \widetilde{C}_0\}$ and $C_1 = \max\{\widehat{C}_1, \widetilde{C}_1\}$, we establish:

$$F(\phi), F_n(\phi) \in [-C_0, C_1].$$

The functional $L(\phi)$ is then decomposed as:

$$L(\phi) = \frac{1}{2}\langle \phi, \mathcal{L}\phi \rangle + F_n(\phi) - 2F(\hat{\phi}) := \frac{1}{2}\langle \phi, \mathcal{L}\phi \rangle + L_n(\phi),$$

where $L_n(\phi) = F_n(\phi) - 2F(\hat{\phi}) \in [-C_0 - 2C_1, 2C_0 + C_1]$. By setting $C = C_0 + 2C_1$, we introduce the auxiliary variable:

$$r(t) = \sqrt{L_n(\phi) + C}.$$

Using the SAV reformulation, the gradient flow equation (4.5) becomes:

$$\begin{cases} \dfrac{\partial \phi}{\partial t} = \Delta \mu, & (4.16a) \\ \mu = \mathcal{L}\phi + \dfrac{r}{\sqrt{L_n(\phi) + C}} \dfrac{\delta L_n}{\delta \phi}(\phi), & (4.16b) \\ \dfrac{\mathrm{d}r}{\mathrm{d}t} = \dfrac{1}{2\sqrt{L_n(\phi) + C}} \left\langle \dfrac{\delta L_n}{\delta \phi}(\phi), \dfrac{\partial \phi}{\partial t} \right\rangle, & (4.16c) \end{cases}$$

subject to appropriate boundary conditions. This formulation preserves the energy dissipation law:

$$\frac{\mathrm{d}L}{\mathrm{d}t} = -\|\nabla \mu\|^2 \leq 0.$$

In fact, taking inner product of(4.16a), (4.16b) and (4.16c) with $\mu, \partial_t \phi$ and $2r$, respectively, and adding them together, we have:

$$\begin{aligned} \frac{\mathrm{d}L}{\mathrm{d}t} &= \left\langle \mathcal{L}\phi, \frac{\partial \phi}{\partial t} \right\rangle + \left\langle 2r, \frac{\mathrm{d}r}{\mathrm{d}t} \right\rangle \\ &= -\|\nabla \mu\|^2 - \frac{r}{\sqrt{L_n(\phi) + C}} \left\langle \frac{\delta L_n}{\delta \phi}, \frac{\partial \phi}{\partial t} \right\rangle + \frac{r}{\sqrt{L_n(\phi) + C}} \left\langle \frac{\delta L_n}{\delta \phi}, \frac{\partial \phi}{\partial t} \right\rangle \\ &= -\|\nabla \mu\|^2 \\ &\leq 0. \end{aligned}$$

4.2.1 First-Order Time Discrete Scheme

The first-order numerical scheme for (4.16) is as follows:

$$\begin{cases} \dfrac{\phi^{n+1} - \phi^n}{\Delta t} = \Delta \mu^{n+1}, & (4.17a) \\ \mu^{n+1} = \mathcal{L}\phi^{n+1} + \dfrac{r^{n+1}}{\sqrt{L_n(\phi^n) + C}} \dfrac{\delta L_n}{\delta \phi}(\phi^n), & (4.17b) \\ \dfrac{r^{n+1} - r^n}{\Delta t} = \dfrac{1}{2\sqrt{L_n(\phi^n) + C}} \left\langle \dfrac{\delta L_n}{\delta \phi}(\phi^n), \dfrac{\phi^{n+1} - \phi^n}{\Delta t} \right\rangle. & (4.17c) \end{cases}$$

Define the modified energy:

$$\overline{L}(\phi, r) = \tfrac{1}{2}\langle \phi, \mathcal{L}\phi \rangle + r^2 - C.$$

Theorem 4.2 *The scheme* (4.17) *is unconditional energy stable with respect to the above modified energy:*

$$\overline{L}(\phi^{n+1}, r^{n+1}) \leq \overline{L}(\phi^n, r^n).$$

Proof Theorem 4.2 *On the one hand, taking inner product of* (4.17a), (4.17b) *and* (4.17c) *with* μ^{n+1}, $\frac{\phi^{n+1}-\phi^n}{\Delta t}$ *and* $2r^{n+1}$, *respectively, we get*

$$\left\langle \frac{\phi^{n+1}-\phi^n}{\Delta t}, \mu^{n+1} \right\rangle = -\|\nabla \mu^{n+1}\|^2, \tag{4.18}$$

$$\begin{aligned}\left\langle \mu^{n+1}, \frac{\phi^{n+1}-\phi^n}{\Delta t} \right\rangle =& \left\langle \mathcal{L}\phi^{n+1}, \frac{\phi^{n+1}-\phi^n}{\Delta t} \right\rangle \\ &+ \frac{r^{n+1}}{\sqrt{L_n(\phi^n)+C}} \left\langle \frac{\delta L_n}{\delta \phi}(\phi^n), \frac{\phi^{n+1}-\phi^n}{\Delta t} \right\rangle,\end{aligned} \tag{4.19}$$

$$\left\langle \frac{r^{n+1}-r^n}{\Delta t}, 2r^{n+1} \right\rangle = \frac{r^{n+1}}{\sqrt{L_n(\phi^n)+C}} \left\langle \frac{\delta L_n}{\delta \phi}(\phi^n), \frac{\phi^{n+1}-\phi^n}{\Delta t} \right\rangle, \tag{4.20}$$

combing the above equalities, we get

$$-\|\nabla \mu^{n+1}\|^2 = \left\langle \mathcal{L}\phi^{n+1}, \frac{\phi^{n+1}-\phi^n}{\Delta t} \right\rangle + \left\langle \frac{r^{n+1}-r^n}{\Delta t}, 2r^{n+1} \right\rangle. \tag{4.21}$$

Thus the energy dissipation law can be obtained

$$\begin{aligned}\overline{L}(\phi^{n+1}, r^{n+1}) - \overline{L}(\phi^n, r^n) &= \frac{1}{2}\left\langle \phi^{n+1}, \mathcal{L}\phi^{n+1} \right\rangle - \frac{1}{2}\langle \phi^n, \mathcal{L}\phi^n \rangle + (r^{n+1})^2 - (r^n)^2 \\ &\leq \left\langle \mathcal{L}\phi^{n+1}, \phi^{n+1} - \phi^n \right\rangle + 2r^{n+1}(r^{n+1} - r^n) \\ &= -\Delta t \|\nabla \mu^{n+1}\|^2 \\ &\leq 0,\end{aligned}$$

by using the inequality

$$(a-b)a \geq \frac{1}{2}\left(|a|^2 - |b|^2\right).$$

The scheme (4.17) can be implemented in three steps:

1. Compute b^n and c^n using their definitions:

$$b^n = \frac{1}{\sqrt{L_n(\phi^n)+C}} \frac{\delta L_n}{\delta \phi}(\phi^n),$$

$$c^n = \phi^n + \Delta t r^n \Delta b^n - \frac{\Delta t}{2}\langle b^n, \phi^n \rangle \Delta b^n.$$

2. Solve for $\langle b^n, \phi^{n+1}\rangle$ from:

$$\left\langle b^n, \phi^{n+1}\right\rangle = \frac{\langle b^n, A^{-1}c^n\rangle}{1+\Delta t\alpha^n/2},$$

where $\alpha^n = -\langle b^n, A^{-1}\Delta b^n\rangle$.

3. Update ϕ^{n+1} using:

$$(I-\Delta t\Delta\mathcal{L})\phi^{n+1} - \frac{\Delta t}{2}\Delta b^n\left\langle b^n, \phi^{n+1}\right\rangle = c^n.$$

4.2.2 Second-Order Numerical Scheme

The unconditionally energy-stable scheme (4.17) allows for large time step sizes; however, increasing the step size can lead to greater numerical errors. To leverage large time steps while ensuring accuracy, it is essential to employ highly accurate, energy-stable schemes. In this section, we propose a second-order backward differentiation formula (BDF) scheme for the system described in (4.16):

$$\begin{cases} \dfrac{3\phi^{n+1}-4\phi^n+\phi^{n-1}}{2\Delta t} = \Delta\mu^{n+1}, & \text{(4.22a)}\\ \mu^{n+1} = \mathcal{L}\phi^{n+1} + \dfrac{r^{n+1}}{\sqrt{L_n(\phi^*)+C}}\dfrac{\delta L_n}{\delta\phi}(\phi^*), & \text{(4.22b)}\\ \dfrac{3r^{n+1}-4r^n+r^{n-1}}{2\Delta t} = \dfrac{1}{2\sqrt{L_n(\phi^*)+C}}\left\langle \dfrac{\delta L_n}{\delta\phi}(\phi^*), \dfrac{3\phi^{n+1}-4\phi^n+\phi^{n-1}}{2\Delta t}\right\rangle, & \text{(4.22c)} \end{cases}$$

where $\phi^* = 2\phi^n - \phi^{n-1}$. This numerical scheme preserves the energy dissipation law as demonstrated below.

Theorem 4.3 *The scheme* (4.22) *is unconditionally energy stable in the sense that*

$$\widetilde{L}\Big[(\phi^{n+1}, r^{n+1}), (\phi^n, r^n)\Big] \le \widetilde{L}\Big[(\phi^n, r^n), (\phi^{n-1}, r^{n-1})\Big],$$

where the modified discrete energy $\widetilde{L}$ *is defined as*

$$\widetilde{L}\Big[(\phi^{n+1}, r^{n+1}), (\phi^n, r^n)\Big] := \frac{1}{4}\Big[\left\langle \phi^{n+1}, \mathcal{L}\phi^{n+1}\right\rangle + \left\langle 2\phi^{n+1}-\phi^n, \mathcal{L}(2\phi^{n+1}-\phi^n)\right\rangle\Big] + \frac{1}{2}\Big[(r^{n+1})^2 + (2r^{n+1}-r^n)^2\Big].$$

Proof Theorem 4.3 *To prove the theorem, we take the inner products of* $2\Delta t\mu^{n+1}$, $3\phi^{n+1}-4\phi^n+\phi^{n-1}$ *and* $2\Delta t r^{n+1}$ *with* (4.22a), (4.22b), *and* (4.22c), *respectively. Using the identity*

$$2\left\langle a^{k+1}, 3a^{k+1}-4a^k+a^{k-1}\right\rangle = \left|a^{k+1}\right|^2 + \left|2a^{k+1}-a^k\right|^2 + \left|a^{k+1}-2a^k+a^{k-1}\right|^2 - \left|a^k\right|^2 - \left|2a^k-a^{k-1}\right|^2,$$

we immediately obtain the desired result.

Remark 4.2 *The unconditional energy stability of the discrete schemes is theoretically established only in terms of the modified energy. However, numerically, both the modified and original energies are shown to decay over time, as demonstrated in the numerical results in section 4.5.1.*

Remark 4.3 *The second-order BDF scheme* (4.22) *can be replaced by the Crank-Nicolson scheme, which offers similar accuracy and stability results. The corresponding scheme is given by:*

$$\begin{cases} \dfrac{\phi^{n+1}-\phi^n}{\Delta t} = \Delta\mu^{n+\frac{1}{2}}, & \text{(4.23a)} \\ \mu^{n+\frac{1}{2}} = \mathcal{L}\dfrac{1}{2}(\phi^{n+1}+\phi^n) + \dfrac{r^{n+1}+r^n}{2\sqrt{L_n(\bar{\phi}^*)+C}}\dfrac{\delta L_n}{\delta\phi}(\bar{\phi}^*), & \text{(4.23b)} \\ \dfrac{r^{n+1}-r^n}{\Delta t} = \dfrac{1}{2\sqrt{L_n(\bar{\phi}^*)+C}}\left\langle \dfrac{\delta L_n}{\delta\phi}(\bar{\phi}^*), \dfrac{\phi^{n+1}-\phi^n}{\Delta t}\right\rangle, & \text{(4.23c)} \end{cases}$$

where $\bar{\phi}^* = (3\phi^n - \phi^{n-1})/2$.

4.3 PROJECTED IMF

This section introduces the Projected IMF, which is designed to improve the performance of IMF methods in locating transition states of energy functional in the H^{-1} metric. The key contribution of this method is the adoption of a projection technique to manage the ill-conditioning that arises when using the H^{-1} metric directly.

The original IMF in the spatially extended system to locate the saddle point of $F(\phi)$ in the H^{-1} metric is represented for comparison:

$$\begin{cases} v^{(k+1)} = \underset{\|v\|_{H^{-1}}=1}{\operatorname{argmin}} \left\langle v, \widetilde{\mathbf{H}}(\phi^{(k)})v\right\rangle_{H^{-1}}, & \text{(4.24a)} \\ \phi^{(k+1)} = \underset{\int_\Omega \phi \ \mathrm{d}\mathbf{x}=m}{\operatorname{argmin}} L(\phi;\phi^{(k)},v^{(k+1)}), & \text{(4.24b)} \end{cases}$$

where $\widetilde{\mathbf{H}} = -\Delta\mathbf{H} = -\delta_\phi^2 F$. $L(\phi) = F(\phi) - 2F(\hat{\phi}), \hat{\phi} = \phi^{(k)} + \left\langle v^{(k+1)}, \phi-\phi^{(k)}\right\rangle_{H^{-1}} v^{(k+1)}$. Because of the mass conservation, the eigenvalue problem (4.24a) is equivalent to

$$\underset{\psi}{\operatorname{argmin}} \left\{ \widetilde{\mathcal{R}}(\psi) : \int_\Omega \psi \,\mathrm{d}x = 0, \quad \|\psi\|_{H^{-1}} = 1 \right\}, \tag{4.25}$$

where $\widetilde{\mathcal{R}}(\psi)$ is the Rayleigh quotient

$$\widetilde{\mathcal{R}}(\psi) = \frac{\left\langle \psi, \widetilde{\mathbf{H}}\psi\right\rangle_{H^{-1}}}{\|\psi\|_{H^{-1}}^2},$$

which is equivalent to finding the smallest eigenvalue of the Hessian of the functional. This step is mathematically complex because the problem involves the H^{-1} inner product, which can lead to ill-conditioning.

The projected IMF is introduced to resolve this ill-conditioning by applying the projection operator $\mathbf{P}$, as discussed in (3.31) in section 3.4. This projection converts the minimization problem into one where the inner product is in the L^2- metric, thus avoiding the direct use of H^{-1} space and simplifying the computations.

The rotation step (4.24a) can be equivalently transformed to

$$v^{(k+1)} = \operatorname{argmin} \langle v, \mathbf{PHP}v \rangle_{L^2},$$

which is also equivalent to the minimization problem

$$\operatorname*{argmin}_{\psi} \left\{ \widehat{\mathcal{R}}(\psi) : \int_\Omega \psi \, \mathrm{d}\mathbf{x} = 0, \quad \|\psi\|_{L^2} = 1 \right\}, \tag{4.26}$$

and the Rayleigh quotient is changed as

$$\widehat{\mathcal{R}}(\psi) = \frac{\langle \psi, \mathbf{PHP}\psi \rangle_{L^2}}{\|\psi\|_{L^2}^2}.$$

So the projected IMF written in terms of $\langle \cdot, \cdot \rangle_{L^2}$ is

$$\begin{cases} v^{(k+1)} = \operatorname*{argmin}_{\|v\|_{L^2}=1} \left\langle v, \widehat{\mathbf{H}}(\phi^{(k)}) v \right\rangle_{L^2}, & \text{(4.27a)} \\ \phi^{(k+1)} = \operatorname*{argmin}_{\int_\Omega \phi(x) \mathrm{d}\mathbf{x} = m} L(\phi; \phi^{(k)}, v^{(k+1)}), & \text{(4.27b)} \end{cases}$$

where $\widehat{\mathbf{H}} = \mathbf{PHP}$. The translation step becomes the gradient flow of the auxiliary functional $L(\phi; \phi^{(k)}, v^{(k+1)})$, leading to the equation:

$$\frac{\partial \phi}{\partial t} = -\mathbf{P} \frac{\delta L}{\delta \phi}(\phi) = -\mathbf{P} \frac{\delta F}{\delta \phi}(\phi) + 2 \left\langle v, \frac{\delta F}{\delta \hat{\phi}}(\hat{\phi}) \right\rangle_{L^2} \mathbf{P}v, \tag{4.28}$$

where

$$\hat{\phi} = \phi^{(k)} + \left\langle v^{(k+1)}, (\phi - \phi^{(k)}) \right\rangle_{L^2} v^{(k+1)}.$$

The dynamics (4.28) automatically enforces mass conservation:

$$\frac{\partial}{\partial t} \int_\Omega \phi(x) \, \mathrm{d}\mathbf{x} = -\int_\Omega \mathbf{P} \frac{\delta L}{\delta \phi} \, \mathrm{d}\mathbf{x} = 0.$$

Thus, the saddle point of $F(\phi)$ in H^{-1} metric can be obtained by solving (4.26) and (4.28). It is easy to find that (4.28) is two orders lower in spatial derivative than that in H^{-1} metric directly. Additionally, the projection eliminates the

need for the inverse of the Laplacian operator Δ^{-1}, which would be required in the H^{-1} metric directly.

Denote the mapping: $\phi^{(k)} \to \phi^{(k+1)}$ in (4.27) as $\Phi(\phi)$, the quadratic convergence rate of the projected IMF can be illustrated by showing the Jacobian matrix of $\Phi(\phi)$ vanishes at the index-1 saddle point.

Theorem 4.4 *Suppose that ϕ^* is a (non-degenerate) index-1 saddle point of the functional $F(\phi)$, $\mathbf{H} = \delta_\phi^2 F$ is continuous. For each ϕ, $v(\phi)$ is the normalized eigenvector corresponding to the smallest eigenvalue of the matrix $\widehat{\mathbf{H}} = \mathbf{PHP}$, i.e.,*

$$v(\phi) = \operatorname*{argmin}_{\|u\|=1} u^T \widehat{\mathbf{H}}(\phi) u.$$

then
(1) *ϕ^* is local minimizer of $L(\phi; \phi^*, v)$;*
(2) *a neighbourhood $\mathcal{U}$ of ϕ^* exists such that for any $\phi \in \mathcal{U}$, $L(\phi; \phi^{(k)}, v)$ is strictly convex w.r.t. $\phi \in \mathcal{U}$ and thus has a unique minimum in $\mathcal{U}$;*
(3) *define the mapping $\Phi : \phi \in \mathcal{U} \to \Phi(\phi) \in \mathcal{U}$ to be the unique minimizer of L in $\mathcal{U}$ for any $\phi \in \mathcal{U}$. Further assume that $\mathcal{U}$ contains no other stationary points of F except for ϕ^*. Then the mapping Φ has only one fixed point ϕ^*;*
(4) *$\Phi(\phi)$ is differentiable in $\mathcal{U}$ and $\mathbf{P}\Phi'(\phi^*)\mathbf{P} = 0$. Thus the iterative mapping $\phi \to \Phi(\phi)$ has a local quadratic convergence rate.*

Proof Theorem 4.4 *The proof of the first three conclusions can be generalized from the finite space to the infinite space based on the proof of Theorem 3.1 in [32] without difficuty. The main difference is the proof of the quadratic convergence rate. Here, we only give the details for the last conclusion.*

In fact, the first order variational derivative of $L(\phi; \phi^{(k)}, v(\phi))$ can be calculated as

$$\delta_\phi L(\phi; \phi^{(k)}, v(\phi)) = \delta_\phi F(\phi) - 2\left\langle v, \delta_{\hat{\phi}} F(\hat{\phi})\right\rangle_{L^2} v.$$

At each $\phi^{(k)} \in \mathcal{U}$, the mapping $\Phi(\phi^{(k)})$ satisfies the first order equation

$$\mathbf{P}\delta_\phi L(\Phi(\phi^{(k)}), \phi^{(k)}, v(\phi^{(k)})) = 0,$$

i.e.,

$$\mathbf{P}\delta_\phi F(\Phi(\phi^{(k)})) - 2\left\langle v(\phi^{(k)}), \delta_{\hat{\phi}} F(\hat{\phi})\right\rangle_{L^2} \mathbf{P} v(\phi^{(k)}) = 0. \tag{4.29}$$

Take derivative w.r.t. $\phi^{(k)}$ on both sides of (4.29), we get

$$\begin{aligned}
&\mathbf{P}^2\mathbf{H}(\Phi(\phi^{(k)}))\mathbf{P}^2\Phi'(\phi^{(k)})\mathbf{P} - 2\left\langle v(\phi^{(k)}), \delta_{\hat{\phi}} F(\hat{\phi})\right\rangle_{L^2} \mathbf{P}^2 J(\phi^{(k)})\mathbf{P} \\
&- 2\left\langle \mathbf{P}J(\phi^{(k)})\mathbf{P}, \delta_{\hat{\phi}} F(\hat{\phi})\right\rangle_{L^2} \mathbf{P} v(\phi^{(k)}) \\
&- 2\left\langle v(\phi^{(k)}), \mathbf{PH}(\hat{\phi})\mathbf{P}\hat{\phi}'\right\rangle_{L^2} \mathbf{P} v(\phi^{(k)}) = 0,
\end{aligned} \tag{4.30}$$

where $J(\phi^{(k)}) = \frac{\partial v(\phi^{(k)})}{\partial \phi^{(k)}}$ *and*

$$\begin{aligned}\hat{\phi}'(\phi^{(k)}) = \mathbf{P} &+ \left\langle v(\phi^{(k)}), \Phi(\phi^{(k)}) - \phi^{(k)} \right\rangle_{L^2} \mathbf{P} J(\phi^{(k)}) \mathbf{P} \\ &+ \left\langle \mathbf{P} J(\phi^{(k)}) \mathbf{P}, \Phi(\phi^{(k)}) - \phi^{(k)} \right\rangle_{L^2} v(\phi^{(k)}) \\ &+ \left\langle v(\phi^{(k)}), \mathbf{P}\Phi'(\phi^{(k)})\mathbf{P} - \mathbf{P} \right\rangle_{L^2} v(\phi^{(k)}).\end{aligned}$$

Let $\phi^{(k)} = \phi^*$ *be the saddle point, we have* $\Phi(\phi^*) = \phi^*, \hat{\phi} = \phi^*, \delta_{\hat{\phi}} F(\phi^*) = 0$ *and* $\hat{\phi}' = \mathbf{P} + \left\langle v(\phi^{(k)}), \mathbf{P}\Phi'(\phi^*)\mathbf{P} - \mathbf{P} \right\rangle_{L^2} v(\phi^*)$, *thus* (4.30) *becomes*

$$\begin{aligned}&\mathbf{P}\mathbf{H}(\phi^*)\mathbf{P}^2\Phi'(\phi^*)\mathbf{P} \\ &= 2\left\langle v(\phi^*), \mathbf{P}\mathbf{H}(\phi^*)\mathbf{P}[\mathbf{P} + \left\langle v(\phi^*), \mathbf{P}\Phi'(\phi^*)\mathbf{P} - \mathbf{P} \right\rangle_{L^2} v(\phi^*)] \right\rangle_{L^2} \mathbf{P} v(\phi^*),\end{aligned}$$

which can be simplified as

$$(\mathbf{P}\mathbf{H}(\phi^*)\mathbf{P} - 2\lambda v v^T)\mathbf{P}\Phi'(\phi^*)\mathbf{P} = 0, \tag{4.31}$$

where $u^T v$ *means* $\langle u, v \rangle$. *By applying* $\mathbf{P}\mathbf{H}\mathbf{P}v = \lambda v$ *and* $\mathbf{P}\mathbf{H}\mathbf{P}(\mathbf{I} - vv^T)\mathbf{P} = 0$. (4.31) *turns out*

$$\mathbf{P}\Phi'(\phi^*)\mathbf{P} = 0.$$

One can carry out the second order derivative of $\Phi(\phi)$ *at* ϕ^* *further and observe that* $\mathbf{P}\Phi''(\phi^*)\mathbf{P} = 0$ *does not trivially hold. Thus the iteration* $\phi \to \Phi(\phi)$ *locally converges to* ϕ^* *with the quadratic rate.*

Remark 4.4 *The mass conservation constraint is linear in this formulation, and the projection* $\mathbf{P}$ *used is a standard orthogonal projection. For more complex nonlinear constraints, the projection may need to be adopted to follow the geodesic distance on the submanifold.*

This approach provides a robust and efficient method for finding transition states in energy landscapes, especially when working with systems defined in function spaces, such as H^{-1}.

4.4 ITERATIVE PROXIMAL MINIMIZATION

In the previous three sections, we explored how transition states can be effectively located using a combination of the convex splitting method and the scalar auxiliary variable (SAV) method, which were integrated into the Iterative Minimization Formulation (IMF). The IMF provides a rigorous mathematical framework for analyzing and improving the numerical methods used to find saddle points of energy functionals. While the IMF demonstrates quadratic convergence in ideal cases, it suffers from limitations such as local convergence and a strong dependence on the quality of initial conditions. Specifically, when the initial guess is far from the region of attraction of the

saddle point, the translation step can lead to divergence with large iteration numbers.

To overcome these challenges, we propose an enhanced algorithm, the Iterative Proximal Minimization (IPM) scheme, which modifies the IMF by incorporating a proximal penalty function. This modification improves the robustness and convergence properties of the algorithm, even when the initial guess is far from the saddle point.

We introduce the following modification to the IMF, incorporating the proximal penalty function:

$$\begin{cases} v^{(k+1)} = \underset{\|u\|=1}{\operatorname{argmin}} u^\top H(x^{(k)})u = v_1(x^{(k)}), & \text{(4.32a)} \\ x^{(k+1)} = \underset{y\in\mathbb{R}^d}{\operatorname{argmin}} L_\rho(y; x^{(k)}, v^{(k+1)}), & \text{(4.32b)} \end{cases}$$

where where the function L_ρ is defined as:

$$\begin{aligned} L_\rho(y; x, v) :=& L(y; x, u) + \rho\ d(x, y) \\ =& (1-\alpha)V(y) + \alpha V\left(y - vv^\top(y-x)\right) \\ & - \beta V\left(x + vv^\top(y-x)\right) + \rho\ d(x,y) \end{aligned} \tag{4.33}$$

with $\rho > 0$ being a positive constant, and $d(x, y)$ is a penalty function on $\mathbb{R}^d \times \mathbb{R}^d$. The auxiliary function L remains as in the original IMF, but the addition of the penalty term $d(x, y)$ ensures that the new formulation encourages a closer proximity between the updated variables $x^{(k+1)}$ and the previous iteration $x^{(k,S)}$ promoting stability and robustness. The penalty function $d(x, y)$ is required to satisfy the following assumptions:

Assumption 1 (Penalty Function)

(a) For any x, $d(x, y)$ is convex and C^2 in y, and

$$\nabla_y^2 d(x, y) = \mathbf{0} \quad \textit{if and only if} \quad y = x;$$

(b) $d(x, y) \geq 0$ for all x, y; and $d(x, y) = 0$ if and only if $x = y$;

(c) For any constant $\epsilon > 0$, there exists a positive constant $\bar{\lambda}_\epsilon > 0$, such that

$$\inf_{\|x-y\|\geq\epsilon} \lambda_{\min}(\nabla_y^2 d(x, y)) \geq \bar{\lambda}_\epsilon.$$

Remark 4.5 *1. The first condition ensures that $d(x, y)$ is convex, but it does not imply strong convexity in y. For example, a function like $\|x-y\|^2$ does not satisfy the first condition. However, functions such as the quartic penalty $d(x, y) = \|x - y\|_4^4 = \sum_{i=1}^d (x_i - y_i)^4$ satisfy all the conditions outlined in* **Assumption** *1. Hence, in the numerical part of the study, we choose the quartic penalty term .*

2. *The second assumption ensures that* $\nabla_y d(x, y) = \mathbf{0}$ *at* $y = x$*, which is crucial for ensuring that the modified functional* L_ρ *retains the same fixed points as the original IMF.*

3. *The third condition guarantees that* $d(x, y)$ *behaves strongly convex outside a small neighborhood around* x*, providing the necessary conditions for the uniqueness of the minimizer of* L_ρ*.*

4. *The penalty function* $d(x, y)$ *is not uniquely determined. For instance, a cubic form could be used instead of the quartic form presented here. A detailed comparison of the effects of these two forms is left to the readers for further exploration.*

We also impose the following assumptions on the potential function V to ensure that the iterative scheme converges to a meaningful solution:

Assumption 2 (Potential Function)

(a) $V \in C^3(\mathbb{R}^d)$ *and is Lipschitz continuous with the Lipschitz constant* $\mathrm{Lip}(V)$*;*

(b) V *has a non-empty and finite set of index-1 saddle points, denoted by* $\mathcal{S}_1$*;*

(c) The Hessian $\nabla^2 V(x)$ *is bounded uniformly, i.e., there exist two constants* $\bar{\lambda}_L$ *and* $\bar{\lambda}_U$ *such that* $\bar{\lambda}_L \leq \lambda_{\min}(\nabla^2 V(x)) \leq \lambda_{\max}(\nabla^2 V(x)) \leq \bar{\lambda}_U$ *for all* $x \in \mathbb{R}^d$*;*

(d) All stationary points of the potential function V *are non-degenerate, meaning that for all* $x \in \mathbb{R}^d$*, the eigenvalues of* $\nabla^2 V(x)$ *are distinct and non-zero.*

Under the above two assumptions, we can derive key properties of the modified auxiliary function L_ρ in the IPM method. To begin, we introduce the mapping $\Phi_\rho : \mathbb{R}^d \to 2^{\mathbb{R}^d}$, which represents the set of global minimizers of the function $L_\rho(y; x, v_1(x))$ for a given $x \in \mathbb{R}^d$.

Definition 4.1 *Let* $\Phi_\rho : \mathbb{R}^d \to 2^{\mathbb{R}^d}$ *be the (set-valued) mapping defined by*

$$x \mapsto \Phi_\rho(x) := \operatorname*{argmin}_{y \in \mathbb{R}^d} L_\rho(y; x, v_1(x)) \tag{4.34}$$

If the optimization problem has no optimal solution, $\Phi_\rho(x)$ *is defined as the empty set. If the optimal solution is not unique,* $\Phi_\rho(x)$ *contains all global minimizers.*

The following theorem characterizes the fixed points of Φ_ρ and their relationship to the index-1 saddle points of the potential function V.

Theorem 4.5 *Assuming* **Assumption** *1 and* **Assumption** *2 hold, the following statements are true:*

(1) There exists a positive constant $\bar{\rho}$, depending on the bounds of $\nabla^2 V$, α and β, such that for all $\rho \geq \bar{\rho}$, we have:

$$\Phi_\rho(x^*) = \{x^*\}, \quad \forall x^* \in \mathcal{S}_1.$$

(2) If $\Phi_\rho(x^*) = \{x^*\}$ with $\rho > 0$, then $x^* \in \mathcal{S}_1$.

Remark 4.6 *The selection of the penalty factor $\bar{\rho}$ is independent of the saddle point x^*, meaning that the algorithm does not require prior knowledge of the saddle point in practice.*

The proof of Theorem 4.5 involves the following proposition and theorem 4.6, and is provided in the Appendix.

Proposition 4.1 *Let V be a continuous Lipschitz function with Lipschitz constant $\mathrm{Lip}(V)$. For any point $x \in \mathbb{R}^d$, any unit vector $\bar{u} \in \mathbb{S}^{d-1}$, and two constants α and β, the function*

$$y \mapsto L(y; x, \bar{u}) = (1-\alpha)V(y) + \alpha V\left(y - \bar{u}\bar{u}^\top (y-x)\right) - \beta V\left(x + \bar{u}\bar{u}^\top (y-x)\right)$$

is Lipschitz continuous with respect to y, and its Lipschitz constant is:

$$\mathrm{Lip}(L) = (|\alpha| + |1-\alpha| + |\beta|)\,\mathrm{Lip}(V)$$

Proof Proposition 4.1 *For each $x \in \mathbb{R}^d$ and $y_1, y_2 \in \mathbb{R}^d$, we have*

$$\begin{aligned}
&\|L(y_1; x, \bar{u}) - L(y_2; x, \bar{u})\| \\
\leq\ & |1-\alpha|\,\|V(y_1) - V(y_2)\| + |\alpha|\left\|V\left(y_1 - \bar{u}\bar{u}^\top (y_1 - x)\right) - V\left(y_2 - \bar{u}\bar{u}^\top (y_2 - x)\right)\right\| \\
&+ |\beta|\,\|V(x + \bar{u}\bar{u}^\top (y_1 - x)) - V(x + \bar{u}\bar{u}^\top (y_2 - x))\| \\
\leq\ & |1-\alpha|\,\mathrm{Lip}(V)\|y_1 - y_2\| + |\alpha|\,\mathrm{Lip}(V)\|(\mathbf{I} - \bar{u}\bar{u}^\top)(y_1 - y_2)\| \\
&+ |\beta|\,\mathrm{Lip}(V)\|\bar{u}\bar{u}^\top (y_1 - y_2)\|.
\end{aligned}$$

Then the conclusion is clear since $\|\mathbf{P}x\| \leq \|x\|$ for any projection matrix $\mathbf{P}$.

The following theorem establishes the existence and uniqueness of minimizers for the optimization problem (4.34) in $\Phi_\rho(x)$ when $x \in \Omega_1$, and demonstrates that these minimizers remain within the index-1 region Ω_1.

Theorem 4.6 *Suppose* **Assumption** *1 and* **Assumption** *2 hold. For any compact subset $\Omega_1' \subset \Omega_1$ and constants $\alpha + \beta > 1$, there exists a positive constant $\bar{\rho} > 0$ depending on α, β, and Ω_1', such that for all $\rho > \bar{\rho}$, the following optimization problem has a unique solution:*

$$\min_{y \in \mathbb{R}^d} L_\rho(y;\, x, v_1(x)) = L(y;\, x, v_1(x)) + \rho \cdot d(x, y). \tag{4.35}$$

This unique solution $\hat{x}$, lies within the index-1 region, i.e., $\Phi_\rho(x) = \{\hat{x}\} \subset \Omega_1$, where $v_1(x)$ is the smallest eigenvector of the Hessian matrix $H(x) = \nabla^2 V(x)$.

The detail proof is left to the Appendix.

A key feature of the proposed method is the incorporation of a non-quadratic penalty function d, satisfying **Assumption** 1, into the auxiliary function existing within the original IMF framework. This modification is straightforward and enhances the convergence behaviour of the algorithm. The principal steps of the Iterative Proximal Minimization (IPM) algorithm are outlined in Algorithm 1. It is important to note that, in practice, the inner minimization subproblems are solved approximately using a suitable stopping criterion. Additionally, when computing transition states in the H^{-1} metric, IPM can be combined with the projection technique discussed in section 4.3, which is further demonstrated through numerical examples.

Algorithm 1 Iterative Proximal Minimization Algorithm

Input: initial guess $x^{(0)}$, $\rho_0 > 0$, $tol > 0$.
Output: saddle point x.
begin
Solve the min-mode $v^{(0)} = \underset{\|u\|=1}{\operatorname{argmin}}\, u^\top H(x^{(0)})u$;
$k = 0$;
while $|\nabla V(x^{(k)})| > tol$ **do**
  $y^{0,k} \leftarrow x^{(k)}$;
  for $i = 0, 1, 2, \cdots, M-1$ **do**
    $y^{i+1,k} = y^{i,k} - \Delta t * \nabla L_\rho(y^{i,k}; x^{(k)}, v^{(k)})$; // gradient descent for L_ρ in (4.33)
  end for
  $k = k + 1$;
  $x^{(k)} \leftarrow y^{M,k}$;
  $v^{(k)} = \operatorname{argmin}_{\|v\|=1} u^\top H(x^{(k)})u$; // solve the minimal eigenvector
end while
return $x^{(k)}$

4.5 NUMERICAL EXAMPLES

In this section, we demonstrate the three proposed methods for locating saddle points using two examples: the one-dimensional Ginzburg–Landau free energy and the two-dimensional and three-dimensional Landau-Brazovskii free energies.

4.5.1 Ginzburg-Landau Free Energy

Consider the one-dimensional Ginzburg–Landau free energy defined on the interval $[0, 1]$:

$$F(\phi) = \int_0^1 \left[\frac{\kappa^2}{2}(\frac{\partial \phi}{\partial x})^2 + f(\phi)\right] \mathrm{d}x, \tag{4.36}$$

where $\phi(x)$ represents an order parameter, such as the concentration of one component in a binary alloy, and $\kappa > 0$ is the mobility parameter. $f(\phi) = (\phi^2 - 1)^2/4$. Two gradient flows are commonly used in physics models, depending on the choice of metric for the gradient:

1. In L^2 metric: the (non-conserved) Allen-Cahn (AC) equation

$$\frac{\partial \phi}{\partial t} = -\frac{\delta F}{\delta \phi}(\phi) = \kappa^2 \Delta \phi - (\phi^3 - \phi); \tag{4.37}$$

and

2. In H^{-1} metric: the (conserved) Cahn–Hilliard (CH) equation:

$$\frac{\partial \phi}{\partial t} = \Delta \frac{\delta F}{\delta \phi} = -\kappa^2 \Delta^2 \phi + \Delta(\phi^3 - \phi). \tag{4.38}$$

Here $\frac{\delta F}{\delta \phi}$ represents the first-order variation of F in the L^2 sense. The Allen-Cahn and Cahn-Hilliard equations are widely used in phase-field models in material sciences and fluid dynamics to model complicated moving interfaces.

We focus on locating the unstable index-1 saddle point of the Ginzburg-Landau free energy (4.36). These saddle points correspond to the "spike-like" stationary solutions, also known as "canonical nuclei," as discussed in [5]. We search for the saddle points of F in both L^2 and H^{-1} metrics.

The auxiliary functional L, as given in (4.2), is modified for the AC and CH equations (with $\alpha = 0$, $\beta = 2$) as follows:

$$L(\phi; \phi^{(k)}, v^{(k+1)}) = F(\phi) - 2F(\hat{\phi}) \tag{4.39}$$

where

$$\hat{\phi} := \phi^{(k)} + \tilde{\phi} = \phi^{(k)} + (v^{(k+1)} \otimes v^{(k+1)})(\phi - \phi^{(k)}). \tag{4.40}$$

Here, $(v \otimes v)u = \langle v, u \rangle v$ for any $u, v,$, and the inner product $\langle \cdot\,, \cdot \rangle$ represents either the L^2-type inner product (for the AC equation) or the $H^{-1}-$type inner product (for the CH equation).

Saddle points in L^2 metric

In the L^2 metric, the second-order variational operator $\mathbf{H}(\phi)$ of the energy functional F, evaluated at ϕ, in the IMF is given by

$$\mathbf{H}(\phi)\psi = \delta_\phi^2 F\, \psi = -\kappa^2 \Delta \psi + f''(\phi)\psi, \quad \forall \psi \in H^2([0,1]),$$

where H^2 is the standard Sobolev space. The eigenvalue problem for this operator

$$\mathbf{H}(\phi)\psi = -\kappa^2 \Delta \psi + f''(\phi)\psi = \lambda \psi, \tag{4.41}$$

subject to boundary conditions, where λ is the eigenvalue. Using the Rayleigh quotient, the eigen-pair for the min-mode, denoted by $\{\lambda_1, \psi_1\}$, solves the following variational problem:

$$\min_{\psi \in H^1([0,1])} \mathcal{R}(\psi) := \frac{\langle \psi, \mathbf{H}\psi \rangle_{L^2}}{\|\psi\|_{L^2}^2} = \frac{\int_0^1 \kappa^2 |\nabla \psi|^2 + f''(\phi)\psi^2 \, \mathrm{d}x}{\int_0^1 |\psi|^2 \, \mathrm{d}x}.$$

After the min-mode is obtained, the subproblem of minimizing the auxiliary functional (4.39) is then solved by evolving the gradient flow:

$$\frac{\partial \phi}{\partial t} = -\frac{\delta L}{\delta \phi}(\phi) = -\frac{\delta F}{\delta \phi}(\phi) + 2(v \otimes v)\frac{\delta F}{\delta \phi}(\hat{\phi}),$$

which leads to the equation

$$\frac{\partial \phi}{\partial t} = \kappa^2 \Delta \phi - \phi^3 + \phi - 2(v \otimes v)(\kappa^2 \Delta \hat{\phi} - \hat{\phi}^3 + \hat{\phi}). \tag{4.42}$$

Here, $v = v^{(k+1)}$ is the min-mode of $\mathbf{H}(\phi^{(k)})$, and $\hat{\phi}$ is defined in (4.40).

Saddle points in H^{-1} metric

In this section, we focus on locating the transition state of $F(\phi)$ in the H^{-1} metric. The relationship between the inner product and norms in the H^{-1} and L^2 metrics is given by:

$$\|\phi\|_{H^{-1}}^2 = \left\langle (-\Delta)^{-1}\phi, \phi \right\rangle_{L^2}, \quad \langle \phi, \psi \rangle_{H^{-1}} = \left\langle (-\Delta)^{-1}\phi, \psi \right\rangle_{L^2}, \tag{4.43}$$

where $(-\Delta)^{-1}$, a bounded positive self-adjoint linear operator, is the inverse of $-\Delta$ subject to certain boundary condition. From this, we can deduce the variational derivatives in the H^{-1} metric:

$$\delta_\phi F\Big|_{H^{-1}} = -\Delta \delta_\phi F, \quad \widetilde{\mathbf{H}} := \delta_\phi^2 F\Big|_{H^{-1}} = -\Delta \delta_\phi^2 F,$$

where $\delta_\phi F$ and $\delta_\phi^2 F$ are the first and second order variational derivatives of $F(\phi)$ in L^2 metric, respectively.

Since mass is conserved in the H^{-1} metric, the eigenvectors or perturbations must belong to the subspace $\left\{\psi : \int_0^1 \psi(x)\mathrm{d}x = 0\right\}$. The eigenvalue problem for $\widetilde{\mathbf{H}}$ is

$$\begin{cases} \widetilde{\mathbf{H}}(\phi)\psi = -\Delta(-\kappa^2 \Delta \psi + f''(\phi)\psi) = \lambda \psi, \\ \quad \int_0^1 \psi(x)\mathrm{d}x = 0, \end{cases} \tag{4.44}$$

subject to Neumann or periodic boundary conditions. For a non-zero eigenvalue, the eigenvector ψ automatically satisfies the condition $\int_0^1 \psi \mathrm{d}x = 0$. For a zero eigenvalue, this condition must be imposed explicitly.

The Rayleigh quotient with respect to H^{-1} metric is:

$$\widetilde{\mathcal{R}}(\psi) = \frac{\left\langle \psi, \widetilde{\mathbf{H}}\psi \right\rangle_{H^{-1}}}{\|\psi\|_{H^{-1}}^2} = \frac{\int_0^1 \kappa^2 |\nabla\psi|^2 + f''(\phi)\psi^2 \,\mathrm{d}x}{\int_0^1 \psi\Delta^{-1}\psi \mathrm{d}x},$$

and the min-mode is the minimizer of the following problem:

$$\operatorname*{argmin}_{\psi} \left\{ \widetilde{\mathcal{R}}(\psi) : \int_0^1 \psi \,\mathrm{d}x = 0, \quad \|\psi\|_{H^{-1}} = 1 \right\}. \tag{4.45}$$

To minimize the auxiliary functional L at each cycle k, the subproblem becomes:

$$\phi^{(k+1)} = \operatorname*{argmin}_{\int_0^1 \phi(x)\mathrm{d}x = m} L(\phi; \phi^{(k)}, v^{(k+1)}), \tag{4.46}$$

where $m = \int_0^1 \phi^{(k)}\mathrm{d}x$, ensuring mass conservation in each IMF cycle. The functional $L(\phi)$ is defined as in (4.40) with the modification of $\hat{\phi}$ given by:

$$\begin{aligned} \hat{\phi} &:= \phi^{(k)} + \left\langle v, \phi - \phi^{(k)} \right\rangle_{H^{-1}} v = \phi^{(k)} + \left\langle -\Delta^{-1}v, \phi - \phi^{(k)} \right\rangle_{L^2} v \\ &= \phi^{(k)} + \left\langle w, \phi - \phi^{(k)} \right\rangle_{L^2} v, \end{aligned} \tag{4.47}$$

Here, $w := -\Delta^{-1}v$ is the unique solution to the equation $-\Delta w = v$, with the additional condition $\int_0^1 w \,\mathrm{d}x = 0$. Then, the variational of $L(\phi)$ is:

$$\delta_\phi L(\phi) = \delta_\phi F(\phi) - 2w \left\langle \delta_\phi F(\hat{\phi}), v \right\rangle_{L^2}.$$

The gradient flow of L in the H^{-1} metric is:

$$\frac{\partial\phi}{\partial t} = \Delta\frac{\delta L}{\delta\phi}(\phi) = \Delta\delta_\phi F(\phi) + 2v \left\langle \delta_\phi F(\hat{\phi}), v \right\rangle_{L^2}, \tag{4.48}$$

which simplifies to the equation:

$$\frac{\partial\phi}{\partial t} = -\kappa^2\Delta^2\phi + \Delta(\phi^3 - \phi) + 2v \left\langle v, -\kappa^2\Delta\hat{\phi} + \hat{\phi}^3 - \hat{\phi} \right\rangle_{L^2}, \tag{4.49}$$

where $v = v^{(k+1)}$ refers to the min-mode of (4.44) at $\phi^{(k)}$, with $\|v\|_{H^{-1}} = 1$. Note that the inner product in (4.48) is in the L^2 sense due to the cancellation of Δ and Δ^{-1}, but the inner product involving $\hat{\phi}$ remains in the H^{-1} metric. This introduces an additional computational cost, as solving for $w = -\Delta^{-1}v$ is required during the IMF subproblem, unlike in the GAD scheme where $\hat{\phi}$ is simply $\phi^{(k)}$ and only one evolution step is needed.

Remark 4.7 *The flow* (4.48) *conserves the mass* $\int_0^1 \phi(x)\mathrm{d}x$*, similar to the CH equation* (4.38)*, and thus the mass constraint in* (4.46) *holds automatically. This means that the IMF mapping* $\phi^{(k)} \to \phi^{(k+1)}$ *does not change the mass at each cycle* k*. To prove this, we integrate both sides of* (4.48) *and use the boundary conditions (Neumann or periodic). The condition* $\int_0^1 v(x)\mathrm{d}x = 0$*, which is the eigenvalue condition for the min-mode* v*, ensures mass conservation.*

In the following numerical test, we set the initial mass $m = 0.6$ for the H^{-1} metric case and search for the transition states satisfying $\int_0^1 \phi(x)\mathrm{d}x = m$.

convex splitting scheme results

In this subsection, we explore the application of the convex splitting method to the saddle point search problems in both the L^2 and H^{-1} metrics. Two convex splitting forms of $F(\phi)$ are discussed in the context of ϕ, given by:

$$F_c^{\mathrm{l}}(\phi) = \int_0^1 \left[\frac{\kappa^2}{2}(\frac{\partial\phi}{\partial x})^2 + \phi^2 + \frac{1}{4}\right]\mathrm{d}x, \quad F_e^{\mathrm{n}}(\phi) = \int_0^1 -\frac{1}{4}\phi^4 + \frac{3}{2}\phi^2\,\mathrm{d}x. \quad (4.50)$$

and

$$\widetilde{F}_c^{\mathrm{n}}(\phi) = \int_0^1 \left[\frac{\kappa^2}{2}(\frac{\partial\phi}{\partial x})^2 + \frac{1}{4}\phi^4 + \frac{1}{4}\right]\mathrm{d}x, \quad \widetilde{F}_e^{\mathrm{l}}(\phi) = \int_0^1 \frac{1}{2}\phi^2\,\mathrm{d}x. \quad (4.51)$$

Remark 4.8 *The functionals in* (4.51) *are always convex, while the second functional* F_e^n *in* (4.50) *is convex only within the region* $\phi \in [-1, 1]$. *In general, when global convexity is not available, to obtain the locally contractive* F_c *and expansive* F_e *terms, one typically introduces a sufficiently large positive constant* C. *For instance the quadratic term* $-\phi^2$ *in the functional* (4.36) *can be written as* $C\phi^2 - (1/2 + C)\phi^2$, *which makes the convex region of* F_e^n *valid for* $\phi^2 \le (2C + 1)/3$. *The form in* (4.50) *corresponds to* $C = 1$.

The L^2 *gradient flow of the Ginzburg-Landau functional ensures that the solution* $\phi(t)$ *always remains in the region* $[-1, 1]$ *by the maximum principle, provided the initial condition satisfies* $|\phi(0)| \le 1$. *However, the* H^{-1} *Cahn-Hillard flow may not necessarily respect this condition, and it is nontrivial to establish such* L_∞ *bounds a prior. For an in-depth theoretical investigation of a convex splitting schemes, we refer to the work in [26], which explores a convex splitting scheme for phase field crystal models. In our numerical simulations, we choose the minimal value* C *such that the local convexity holds for the initial configuration. Empirically, we did not observe unstable phenomena in the two test cases considered here. However, it should be noted that this choice of* C *lacks a theoretic foundation and cannot be guaranteed to work in all situations.*

We consider both the Neumann and periodic boundary conditions. For the AC equation, the Neumann boundary condition is given by:

$$\partial_x\phi(0) = \partial_x\phi(1) = 0,$$

while for the Cahn-Hilliard (CH) equation, the Neumann boundary conditions are:

$$\partial_x\phi(0) = \partial_x\phi(1) = \partial_x^3\phi(0) = \partial_x^3\phi(1) = 0.$$

The periodic boundary condition simply requires that $\phi(x) = \phi(x + 1),\ \forall x \in [0, 1]$, which induces a degeneracy at any stationary solution due to the invariance of translation in the spatial variable, i.e., $\phi(x) \to \phi(x + c)$. This means

that the second smallest eigenvalue of the index-1 saddle points is zero. Despite this degeneracy, the quadratic convergence rate of the IMF method is unaffected by the boundary condition. It is improtant to note that the mass $\int_0^1 \phi(x)dx$ is conserved in the H^{-1} metric, and any stationary solution remains stationary if an arbitrary constant is added. This degeneracy can be eliminated by restricting the solutions to a subspace where the mass is fixed a priori. For the same reason, any eigenvectors or perturbations should be restricted to have zero mass. Further details regarding this degeneracy and the impact of boundary conditions on the solution will be discussed later in the text. It is also worth noting that the existence of a simple index-1 saddle point under Neumann boundary conditions for the AC or CH equations is theoretically guaranteed for sufficient small κ for the double well potential. For more details, we refer the reader to [4, 5] and references therein. In our calculations, we restrict our analysis to cases with not too large domains, i.e., where the parameter κ in (4.36) is small enough to posses saddle points bu not too small to make the domain excessively large.

Convex Splitting Scheme. By substituting (4.50) and (4.51) into different instances of F in $L(\phi)$, we obtain the convex splitting form of $L(\phi)$:

$$L(\phi) = \left[F_c^{\mathrm{l}}(\phi) + 2\,\widetilde{F}_e^{\mathrm{l}}(\hat{\phi})\right] - \left[F_e^{\mathrm{n}}(\phi) + 2\,\widetilde{F}_c^{\mathrm{n}}(\hat{\phi})\right] =: L_c(\phi) - L_e(\phi),$$

where

$$\begin{aligned} L_c(\phi) &= \int_0^1 \left[\frac{\kappa^2}{2}(\phi_x)^2 + \phi^2 + \frac{1}{4} + \hat{\phi}^2\right] \mathrm{d}x, \\ L_e(\phi) &= \int_0^1 \left[-\frac{1}{4}\phi^4 + \frac{3}{2}\phi^2 \ + \kappa^2(\hat{\phi}_x)^2 + \frac{1}{2}\hat{\phi}^4 + \frac{1}{2}\right] \mathrm{d}x. \end{aligned}$$

Here, $\hat{\phi}$ is defined in (4.47). The first order variational derivatives of $L_c(\phi)$ and $L_e(\phi)$ are

$$\begin{aligned} \delta_\phi L_c(\phi) &= -\kappa^2\Delta\phi + 2\phi + 2(v\otimes v)\hat{\phi}, \\ \delta_\phi L_e(\phi) &= -\phi^3 + 3\phi + 2(v\otimes v)\left(-\kappa^2\Delta\hat{\phi} + \hat{\phi}^3\right), \end{aligned}$$

in the L^2 metric, and

$$\begin{aligned} \delta_\phi L_c(\phi) &= -\kappa^2\Delta\phi + 2\phi + 2\left\langle v, \hat{\phi}\right\rangle_{L^2} w, \\ \delta_\phi L_e(\phi) &= -\phi^3 + 3\phi + 2\left\langle -\kappa^2\Delta\hat{\phi} + \hat{\phi}^3, v\right\rangle_{L^2} w, \end{aligned}$$

in the H^{-1} metric. Thus, the convex splitting scheme for (4.42) in the L^2 metric is:

$$\begin{aligned} \frac{\phi^{n+1}-\phi^n}{\Delta t} =& \left[\kappa^2\Delta\phi - 2\phi - 2(v\otimes v)\phi\right]^{n+1} \\ &+ \left[-\phi^3 + 3\phi + 2(v\otimes v)\left(-\kappa^2\Delta\hat{\phi} + \hat{\phi}^3\right)\right]^n, \end{aligned} \tag{4.52}$$

with $\langle v, v\rangle_{L^2} = 1$ and $(v \otimes v)\hat{\phi} = (v \otimes v)\phi$, while the convex splitting scheme for (4.49) in the H^{-1} metric is:

$$\begin{aligned}\frac{\phi^{n+1} - \phi^n}{\Delta t} =& \left[-\kappa^2\Delta^2\phi^{n+1} + 2\Delta\phi^{n+1} - 2\left\langle w, \phi^{n+1}\right\rangle_{L^2}\langle v, v\rangle_{L^2} v\right] \\ & - 2\left\langle v, \phi^{(k)}\right\rangle_{L^2} v + 2\left\langle w, \phi^{(k)}\right\rangle_{L^2}\langle v, v\rangle_{L^2} v \\ & + \left[\Delta(\phi^n)^3 - 3\Delta\phi^n + 2\left\langle v, -\kappa^2\Delta\hat{\phi}^n + (\hat{\phi}^n)^3\right\rangle_{L^2} v\right],\end{aligned} \tag{4.53}$$

where $v = v^{(k+1)}$, $w = -\Delta^{-1}v^{(k+1)}$ and $\hat{\phi}^n$ is from (4.47) with $\phi = \phi^n$.

Non-convex-splitting Scheme. For comparison, We utilize traditional semi-implicit schemes, which are not in the form of a convex splitting method. The non-convex splitting scheme (nCS) is derived by linearizing the nonlinear terms. The following two nCS schemes correspond to the L^2 and H^{-1} metrics:

$$\begin{aligned}\frac{\phi^{n+1} - \phi^n}{\Delta t} =& \kappa^2\Delta\phi^{n+1} + \phi^{n+1} - \left([\phi^n]^3 + 3[\phi^n]^2(\phi^{n+1} - \phi^n)\right) \\ & - 2\left[\langle v, \kappa^2\Delta\hat{\phi} - \hat{\phi}^3 + \hat{\phi}\rangle v\right]^n.\end{aligned} \tag{4.54}$$

$$\begin{aligned}\frac{\phi^{n+1} - \phi^n}{\Delta t} =& -\kappa^2\Delta^2\phi^{n+1} - \Delta\phi^{n+1} + \Delta\left[(\phi^n)^3 + 3[(\phi^n)^2(\phi^{n+1} - \phi^n)]\right] \\ & - 2\left[\langle v, \kappa^2\Delta\hat{\phi} - \hat{\phi}^3 + \hat{\phi}\rangle v\right]^n.\end{aligned} \tag{4.55}$$

In numerical tests for the L^2 metric case, we use $\kappa = 0.01$ and the finite difference method with the mesh grid $\{x_i = ih, i = 0, 1, 2, \ldots, N\}$, where $h = 1/N$ and $N = 200$. A finer mesh with $N = 1000$ is also used to verify the results. Two homogeneous constant states: $\phi_+(x) \equiv 1$ and $\phi_-(x) \equiv -1$, are the only steady states of the free energy $F(\phi)$ in the L^2 metric, regardless of boundary conditions.

For the Neumann boundary condition(NBC), there are two transition states for different initial conditions: $\phi_0(x) = \cos\pi x$ and $\phi_0(x) = \cos 2\pi x$, as shown in Fig. 4.1 **a** and **b**, respectively. The later has two transition layers and a higher free energy than the former, which has only one single layer. For the periodic boundary condition(PBC), with initial condition $\phi_0(x) = \sin 2\pi x$, the transition state is displayed in Fig. 4.1**c**, which is a translation of the transition state in Fig. 4.1 **b**. The numerical results have been published in [42].

Fig. 4.2 shows the quadratic convergence rate of the IMF for both boundary conditions [42], consistent with the theoretical results. In the computation, each subproblem is solved with extremely high precision to ensure convergence.

In order to compare the performance of the convex splitting (CS) scheme (4.52) with the non-convex splitting (nCS) scheme (4.54), we examine three aspects. First, we compare the number of iterations required by the CSS and nCSS to attain the same error tolerance $err := \|\delta_\phi L(\phi^n)\|_{L^2}$ within a fixed cycle. Results for the first cycle, with tolerance values of $1.0 \times 10^{-4}, 1.0 \times$

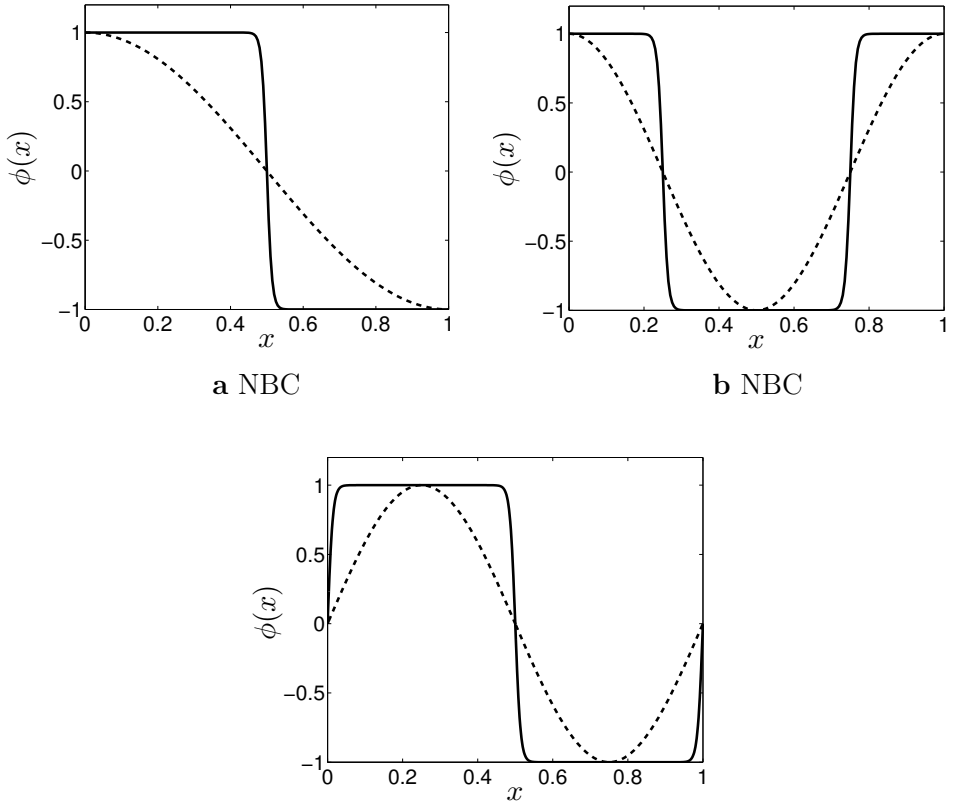

a NBC

b NBC

c PBC

Figure 4.1 Profiles of some saddle points (solid lines) of $F(\phi)$ in L^2 metric computed from various initial states (dashed lines). **a** and **b:** the Neumann boundary condition; **c**: the periodic boundary condition. The free energy F for these three plotted states from left to right are 0.0094, 0.0188, and 0.0188, respectively. $\kappa = 0.01$.

10^{-6} and 1.0×10^{-8} are shown in Table 4.1. The CS scheme shows better stability than the nCS scheme, especially when using a large time step size (with divergence indicated by ∞), and requires fewer iterations to achieve the same accuracy [42].

The second comparison focuses on the overall efficiency in locating the transition state. Specifically, we fix the number of inner iterations and compare the required outer cycles to reach the given error tolerance, defined by $\left\|\delta_\phi F(\phi^{(k)})\right\|_{L^2}$. The total computational cost is then defined as the product of the inner iteration count ("iter#") and the number of outer cycles. The results are summarized in Table 4.2, from which two key conclusions emerge: (1) For both boundary conditions, the CS scheme exhibits a reduction in total computational cost with increasing time step size, whereas the nCS scheme becomes divergent for large time step sizes; (2) When using very small time

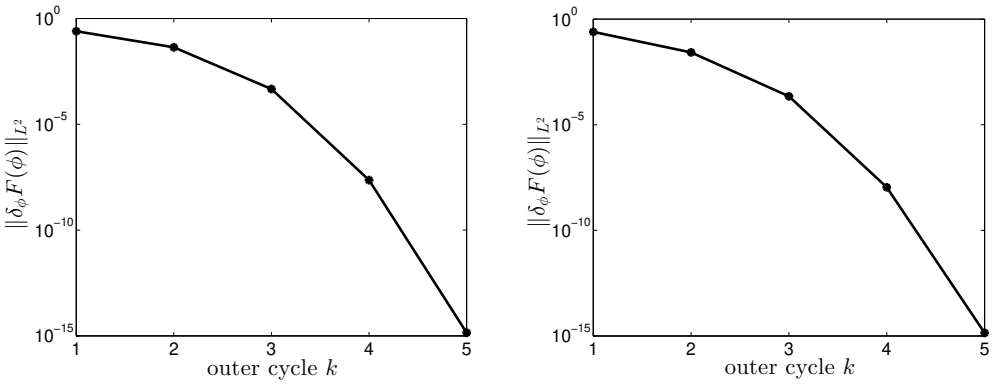

a NBC **b PBC**

Figure 4.2 The validation of the quadratic convergence rate of the IMF mapping Φ by plotting the decay of the error, measured by the force $\|\delta_\phi F(\phi^{(k)})\|_{L^2}$ at each cycle k.

TABLE 4.1 The comparison of the CS scheme (4.52) and nCS scheme (4.54) for the subproblem within the first cycle $\phi^{(0)} \to \phi^{(1)} = \Phi(\phi^{(0)})$. The integers shown in the table are the required number of iterations for (4.52) and (4.54) to achieve the prescribed error tolerance $\|\delta_\phi L(\phi^n)\|_{L^2} \le 10^{-4}, 10^{-6}$, and 10^{-8}.

Δt	The required number of iterations					
	err $= 10^{-4}$		err $= 10^{-6}$		err $= 10^{-8}$	
	(4.52)	(4.54)	(4.52)	(4.54)	(4.52)	(4.54)
0.01	777	763	1092	1074	1407	1386
0.1	92	78	129	111	166	144
5.0	16	∞	23	∞	30	∞
10	14	∞	21	∞	28	∞

a NBC. The initial state is $\phi^{(0)} = \cos \pi x$.

Δt	The required number of iterations					
	err $= 10^{-4}$		err $= 10^{-6}$		err $= 10^{-8}$	
	(4.52)	(4.54)	(4.52)	(4.54)	(4.52)	(4.54)
0.01	728	722	1043	1034	1358	1347
0.1	86	74	123	108	160	141
5.0	14	∞	22	∞	29	∞
10	13	∞	20	∞	27	∞

b PBC. The initial state is $\phi^{(0)} = \sin 2\pi x$.

TABLE 4.2 The comparison of the required number of outer cycles for the CS scheme (4.52) and the nCS scheme (4.54) to attain the given error tolerance $\|\delta_\phi F(\phi^{(k)})\|_{L^2} \le 10^{-8}$ when the inner iteration number is fixed as 50, 80, and 100, respectively, for different time step sizes.

Δt	The number of cycles					
	iter $\# = 50$		iter $\# = 80$		iter $\# = 100$	
	(4.52)	(4.54)	(4.52)	(4.54)	(4.52)	(4.54)
0.01	29	28	18	18	15	14
0.1	4	3	3	2	2	2
5.0	1	∞	1	∞	1	∞

a NBC. The initial state is $\phi^{(0)} = \cos \pi x$.

Δt	The number of cycles					
	iter $\# = 50$		iter $\# = 80$		iter $\# = 100$	
	(4.52)	(4.54)	(4.52)	(4.54)	(4.52)	(4.54)
0.01	28	27	17	17	14	14
0.1	4	3	3	2	2	2
5.0	1	∞	1	∞	1	∞

b PBC. The initial state is $\phi^{(0)} = \sin 2\pi x$.

step sizes, such as $\Delta t = 0.01$, there is little difference in the computational cost between the CS and nCS schemes [42].

Finally, to better visualize the improvement of the CS scheme over the nCS scheme, we plot the decay of the error $\|\delta_\phi F(\phi)\|_{L^2}$ with respect to the total iteration number, as shown in Fig. 4.3. This plot illustrates the trade-off between the accuracy (the vertical axis) and the total computational cost (the horizontal axis). The solid lines represent results from the CS scheme, while the dashed lines correspond to the nCS scheme [42]. It is important to note that the step sizes used for the CS and nCS schemes differ in order to achieve this efficiency gain.

In the numerical test for the H^{-1} metric case, with $N = 200$ and $\kappa = 0.04$, the function $\phi(x)$ is represented by the vector $\boldsymbol{\phi} = (\phi_0, \phi_1, \phi_2, \ldots, \phi_N)^T$ for the Neumann boundary condition, and by $\boldsymbol{\phi} = (\phi_0, \phi_1, \phi_2, \ldots, \phi_{N-1})^T$ for the periodic boundary condition, where $\phi_i \approx \phi(x_i)$. The matrix form of the Hessian matrix $\widetilde{\mathbf{H}}$ at the state $\boldsymbol{\phi}$ is given by $\widetilde{\mathbf{H}}(\boldsymbol{\phi}) = A\nabla^2 F_h(\boldsymbol{\phi})$, where $\nabla^2 F_h(\boldsymbol{\phi}) = \frac{\partial^2 F_n}{\partial \phi_i \partial \phi_j}$. A and $F_h(\boldsymbol{\phi})$ represent the discretized forms of the operator $-\Delta$ and the potential energy $F(\phi)$, respectively. According to (4.44), the equivalent form of $\widetilde{\mathbf{H}}$ is $\kappa^2 A^2 + A\,\mathrm{diag}\{f''(\boldsymbol{\phi})\}$. The min-mode v of the Hessian matrix $\widetilde{\mathbf{H}}$ can be calculated using the Rayleigh quotient in (4.45).

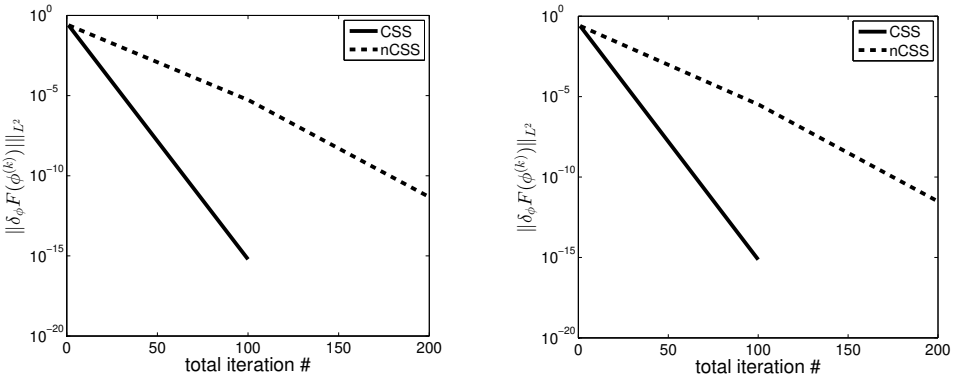

a NBC **b PBC**

Figure 4.3 The decay of the error measured by the gradient $\|\delta_\phi F(\phi^{(k)})\|_{L^2}$ with the total iteration number (i.e., the cost) for the CS scheme (4.52) (solid line) and the nCS scheme (4.54) (dashed line). The inner iteration number in each cycle is fixed as 100 and the time step sizes are $\Delta t = 5.0$ and 0.1 for the CS and nCS schemes, respectively.

Fig. 4.4 shows the stationary states of the free energy $F(\phi)$ in the H^{-1} metric with the Neumann boundary condition [42]. In Fig. 4.4**a**, two metastable states are shown, while Fig. 4.4**b** shows the transition state (solid line) compared to the initial state (dashed line). Fig. 4.5 shows the stationary states of $F(\phi)$ in the H^{-1} metric for the periodic boundary condition [42]. These results are consistent with those reported in [113]. It is worth noting that for the Neumann boundary condition, there are additional stationary states obtainable through symmetric reflection $\phi(x) \to \phi(1-x)$ or with higher indices, which are not shown in Fig. 4.4. The quadrate convergence rate of the IMF for the H^{-1} case is further validated in Fig. 4.6, where the error is measured by the force in the H^{-1} metric:

$$err := \left\| \delta_\phi F(\phi^{(k)})|_{H^{-1}} \right\|_{H^{-1}} = \left\| -\Delta \delta_\phi F(\phi^{(k)}) \right\|_{H^{-1}}.$$

To demonstrate the advantage of the CSS over the nCSS, we compare the performance of the CS scheme in (4.53) with the nCS scheme in (4.55). As in the L^2 metric case, we begin by examining the performance for the subproblem. For the first cycle, Table 4.3 compares the inner iteration numbers required to minimize L for both schemes, in order to reach three error tolerances: $\|\Delta \delta_\phi L\|_{H^{-1}} \le 1.0 \times 10^{-4}, 1.0 \times 10^{-5}$ and 1.0×10^{-6}. The results show similar trends to the L^2-metric case. When both the CS and nCS schemes converge for a small time step, the nCS scheme requires fewer iterations to reach the same tolerance, particularly for the periodic boundary condition. This is possible become a more stable scheme does not necessarily lead to a faster convergence rate towards the minimum. The key takeaway from this

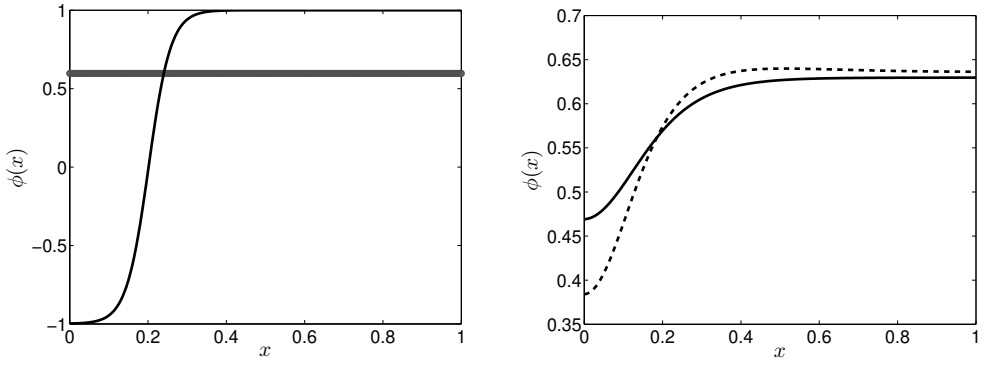

a Two stable states **b Transition state**

Figure 4.4 (NBC. H^{-1} metric.) **a**: two stable stationary states of $F(\phi)$ with the mass $\int_0^1 \phi\, dx = 0.6$. $F = 0.10240$ for the trivial constant state (the thick line) and $F = 0.03772$ for the transition layer state (the thin line). **b**: the transition states (solid line) with the free energy 0.10241 whose first three eigenvalues are $\lambda = -3.41, 3.91$, and 18.14, calculated from the initial condition (dashed line) whose first three eigenvalues are $\lambda = -10.97, 3.45$, and 17.48. Note that the vertical axes in subfigures **a** and **b** are in different scales.

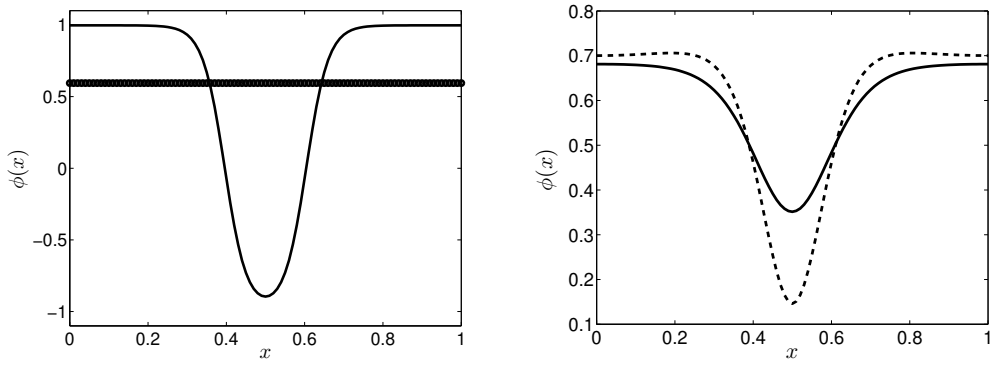

a Two stable states **b Transition state**

Figure 4.5 (PBC. H^{-1} metric.) **a**: the two stable stationary states of $F(\phi)$ in H^{-1} metric with the given mass $\int_0^1 \phi\, dx = 0.6$. $F = 0.10240$ for the constant state and $F = 0.07510$ for the other non-constant state. **b**: one of the transition states (solid line) with the free energy 0.10285 whose first three smallest (numerical) eigenvalues are $-12.75, -1.86 \times 10^{-7}$ (corresponding to theoretical zero eigenvalue), and 46.15. The initial state is shown as the dashed line in which the first three smallest eigenvalues are $\lambda = -27.13, -6.81$, and 44.98. $\kappa = 0.04$. Note the different scales in the vertical axes.

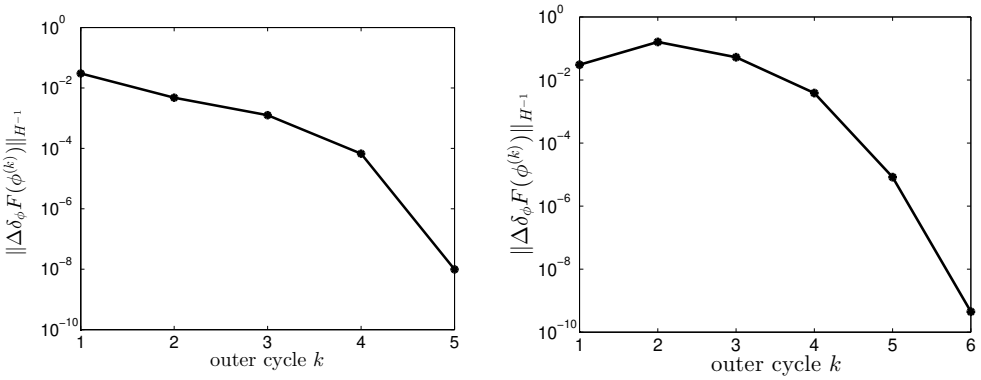

a NBC **b PBC**

Figure 4.6 The quadratic convergence rate of the IMF mapping by plotting the decay error, measured by $\|\Delta\delta_\phi F(\phi)\|_{H^{-1}}$ at each cycle k. The corresponding initial states are specified in Fig. 4.4**a** and 4.4**b**, respectively.

comparison is that, for both the CS and nCS schemes, a larger time step size results in fewer iterations, provided the results still converge.

Table 4.4 represents the overall performance of the convex splitting scheme in the H^{-1} metric. The conclusions drawn from this table are qualitatively

TABLE 4.3 The comparison of the CS scheme (4.53) and nCS scheme (4.55) for the subproblem $\phi^{(0)} \to \phi^{(1)} = \Phi(\phi^{(0)})$. The integers shown in the table are the required number of iterations to achieve the three prescribed tolerances $\|\Delta\delta_\phi L(\phi^n)\|_{H^{-1}} \le 10^{-4}, 10^{-5}$, and 10^{-6}.

Δt	The required number of iterations					
	err	$= 10^{-4}$	err	$= 10^{-5}$	err	$= 10^{-6}$
	(4.53)	(4.55)	(4.53)	(4.55)	(4.53)	(4.55)
10^{-3}	2956	2647	3332	2993	3709	3339
10^{-2}	550	273	617	308	685	343
10^{-1}	283	∞	321	∞	360	∞
1.0	14	∞	262	∞	298	∞

a NBC.

Δt	The required number of iterations					
	err	$= 10^{-4}$	err	$= 10^{-5}$	err	$= 10^{-6}$
	(4.53)	(4.55)	(4.53)	(4.55)	(4.53)	(4.55)
10^{-3}	1022	820	1163	939	1305	1057
10^{-2}	281	77	316	88	351	99
10^{-1}	208	∞	233	∞	257	∞

b PBC.

TABLE 4.4 The comparison of the number of outer cycles required for the CS scheme (4.53) and the nCS scheme (4.55) to attain the given error tolerance $\|\Delta\delta_\phi F(\phi^{(k)})\|_{H^{-1}} \leq 10^{-8}$, when the inner iteration number is fixed for the different choices of the time step size $\Delta t = 10^{-3}, 10^{-2}$, and 10^{-1}. The corresponding initial states are specified in Fig. 4.4**b** and Fig. 4.5**b**, respectively.

Δt	The number of cycles					
	iter $\# = 40$		iter $\# = 50$		iter $\# = 60$	
	(4.53)	(4.55)	(4.53)	(4.55)	(4.53)	(4.55)
10^{-3}	118	102	95	82	79	69
10^{-2}	28	∞	22	∞	16	∞
10^{-1}	16	∞	17	∞	16	∞

a NBC.

Δt	The required number of iterations					
	iter $\# = 50$		iter $\# = 80$		iter $\# = 100$	
	(4.53)	(4.55)	(4.53)	(4.55)	(4.53)	(4.55)
10^{-3}	34	25	22	16	18	13
10^{-2}	13	∞	7	∞	8	∞
10^{-1}	11	∞	8	∞	7	∞

b PBC.

consistent with those in Table 4.2. Finally, the evolution of the error, measured by the force $\|\Delta\delta_\phi F(\phi^{(k)})\|_{H^{-1}}$, as a function of the total computational cost (i.e., the total number of iterations) is plotted for both the CSS and the nCSS schemes. The optimal time step sizes for each method are chosen based on the data in Table 4.4, and resulting comparison is shown in Fig. 4.7, which highlights the robustness of the method with respect to the initial states [42]. Specifically, random perturbations are added to the initial guess, resulting in multiple curves that exhibit the same overall behaviour.

Scalar auxiliary variable results

In this section, we apply the Scalar Auxiliary Variable (SAV) approach to locate the saddle point of the Ginzburg-Landau free energy in the H^{-1} metric.

To solve the dynamics described by equation (4.49) efficiently using the schemes (4.17) and (4.22), we define the operator $\mathcal{L}$ and the energy functional L_n as follows:

$$\mathcal{L} = -\kappa^2\partial_x^2, \qquad L_n = \int_0^1 \frac{(\phi^2-1)^2}{4} - \kappa^2(\frac{\partial\hat{\phi}}{\partial x})^2 - \frac{(\hat{\phi}^2-1)^2}{2}\mathrm{d}x.$$

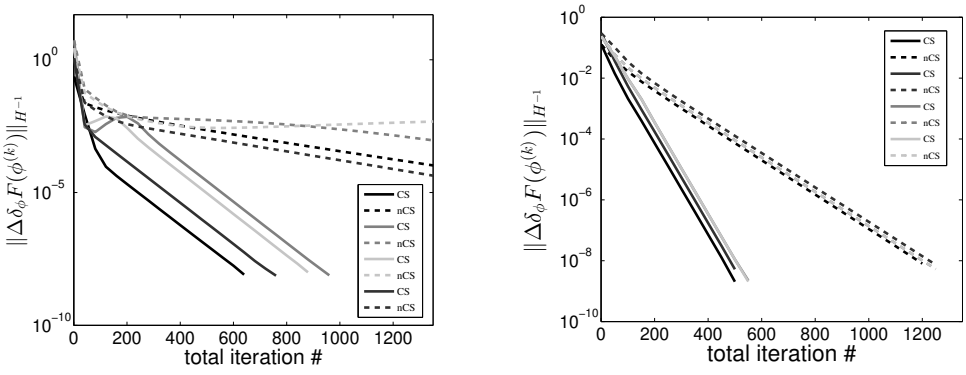

a NBC **b PBC**

Figure 4.7 The evolution of the errors measured by $\|\Delta\delta_\phi F(\phi)\|_{H^{-1}}$ w.r.t. the total iteration number for the CS scheme (4.53) (solid lines) and the nCS scheme (4.55) (dashed lines). Different small perturbations around the initial condition used in Table 4.4 are added as the new initial conditions here to produce multiple lines. For the Neumann boundary condition in **a**, the inner iteration number is 40 and the time step sizes are $\Delta t = 10^{-1}$ and 10^{-3} for the CS and nCS schemes, respectively. For the periodic boundary condition in **b**, the inner iteration number is 50. The time step sizes are the same as in **a**.

The corresponding variational derivative is:

$$\frac{\delta L_n(\phi)}{\delta\phi} = \phi^3 - \phi - 2v\left\langle w, -\kappa^2\partial_x^2\hat{\phi} + \hat{\phi}^3 - \hat{\phi}\right\rangle.$$

In the numerical tests, we set $\kappa = 0.04$. We begin by validating the accuracy of the proposed schemes (4.17) and (4.22) for solving the gradient flow equation (4.49) over one cycle in the IMF. Table 4.5 presents the convergence order of the two numerical schemes [39], calculated using the formula:

$$\log[e(\Delta t)/e(\Delta t/2)],$$

where $e(\Delta t) = \|\phi - \phi^*\|_{L^2}$, and ϕ^* is the reference solution, computed with $\Delta t = 10^{-5}$ using scheme (4.22). The numerical solution ϕ is obtained with the time step size Δt. We test various time step sizes: $\Delta t = 1.6 \times 10^{-3}$, 8×10^{-4}, 4×10^{-4}, 2×10^{-4}, 10^{-4} at $t = 0.01$. It is important to note that the convergence order discussed here refers to the rate at which the numerical solution converges to the steady states of the gradient flow, rather than the overall convergence rate of the entire algorithm.

Additionally, we demonstrate the energy stability of the scheme over one cycle by using a grid spacing of $\Delta x = 0.01$ and a time step size of $\Delta t = 10^{-4}$. Fig. 4.8**a** shows the energy decay over time for both the modified energy and original energy [39], as computed by scheme (4.17). The results obtained

TABLE 4.5 Temporal errors and orders of convergence for ϕ at $t = 0.01$ with fixed $\Delta x = 10^{-5}$ and different temporal step sizes Δt in one cycle in the IMF. The l_2 norm error $e(\Delta t)$ is computed by comparing with the reference solution obtained by the second-order scheme with $\Delta t = 10^{-5}$. The order is calculated through the formula $\log[e(\Delta t)/e(\Delta t/2)]$.

Scheme	$\Delta t =$	1.6e-3	8e-4	4e-4	2e-4	1e-4
1st-order	Error	1.57e-2	8.35e-3	4.29e-3	2.16e-3	1.07e-3
	Order	-	0.91	0.96	0.99	1.01
2nd-order	Error	5.13e-4	1.39e-4	3.58e-5	8.89e-6	2.18e-6
	Order	-	1.88	1.96	2.01	2.03

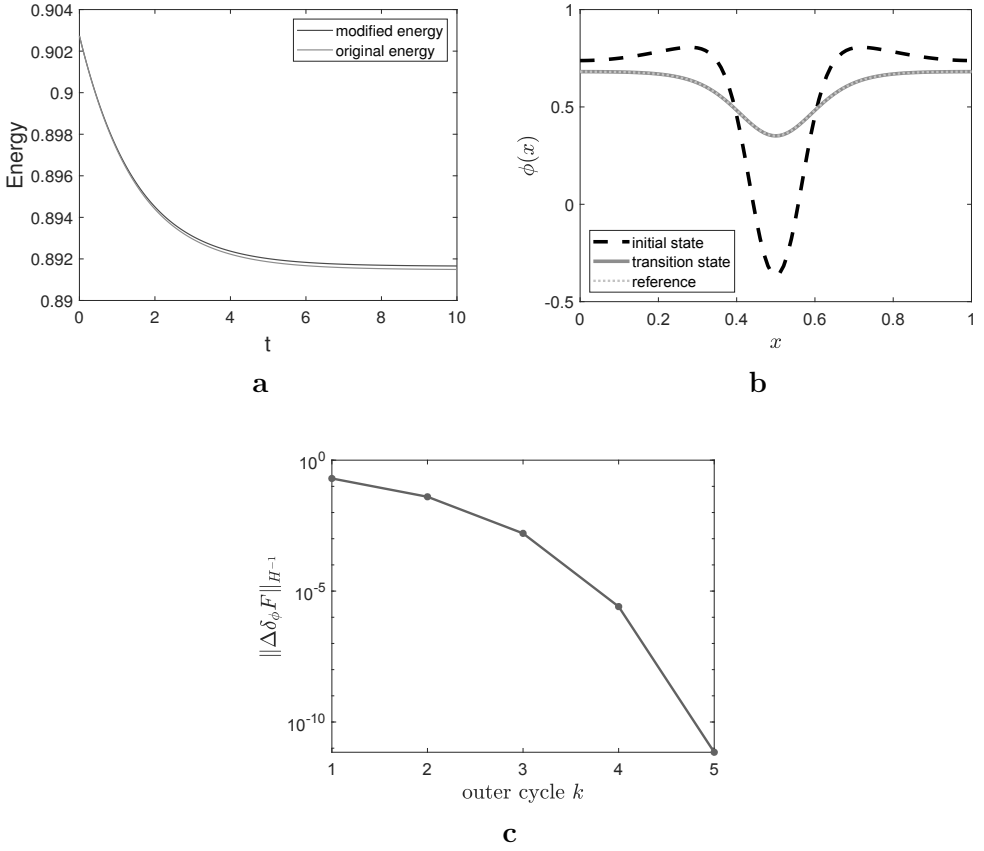

Figure 4.8 **a** is the evolution of original energies (grey line) and modified energies (black line) obtained by the first-order scheme (4.17) in the first cycle of the IMF; **b:** initial state (dashed line), transition state obtained by the IMF-SAV (grey solid line), reference solution obtained by the string method (grey dotted line); **c:** quadratic convergence rate of the IMF-SAV. The error is measured by the force $\|\Delta\delta_\phi F\|_{H^{-1}}$.

from scheme (4.22) are almost identical to those shown in Fig. 4.8**a**. Fig. 4.8**b** presents the saddle point of the free energy $F(\phi)$ in the H^{-1} metric [39], as obtained using the IMF-SAV method (red solid line). This result matches exactly with the one obtained using the string method (green dashed line). Finally, Fig. 4.8**c** illustrates the quadratic convergence rate of the IMF-SAV method [39], with the error measured by the force $\|\Delta\delta_\phi F\|_{H^{-1}}$.

Furthermore, to highlight the advantages of the IMF-SAV method, we compare its performance against two other approaches: the IMF-GD (where the translation step is handled using the gradient descent method) and the IMF-SI (where the translation step is treated using a semi-implicit scheme). The semi-implicit scheme is formulated as follows:

$$\frac{\phi^{n+1}-\phi^n}{\Delta t} = -\kappa^2\partial_x^4\phi^{n+1} + \partial_x^2\left(\phi^n\right)^3 - \partial_x^2\phi^n + 2\left\langle v, -\kappa^2\partial_x^2\hat{\phi}^n + (\hat{\phi}^n)^3 - \hat{\phi}^n\right\rangle v,$$

where $v = v^{(k+1)}$. The comparison is made from two perspectives:

1. Performance of the Subproblem:
   We first compare the performance of the subproblem $\operatorname{argmin}_\phi L(\phi; \phi^{(k)}, v^{(k+1)})$ for three schemes. Specifically, we examine the number of iterations each scheme requires to achieve the same error tolerance *tol*. Table 4.6 shows the comparison results for $tol = 10^{-4}$ and 10^{-6}, with the error measured by $\|\delta_\phi L\|_{H^{-1}}$ [39]. A value of "∞" indicates that the computational solution diverges. The table highlights the super stability and efficiency of the IMF-SAV method compared to the other two schemes.

2. Overall Efficiency:
   The second comparison evaluates the overall efficiency of the three schemes in locating transition states. In this case, we fix the number of inner iterations per cycle and compare the number of outer cycles required to achieve the same tolerance, $\|\delta_\phi F\|_{H^{-1}} \le 10^{-8}$. As shown in Table 4.7, although the IMF-SAV requires slightly more outer cycles than the IMF-SI method for small time step sizes, it enables the use of larger time step sizes, which drastically reduces the number of outer cycles. In contrast, the other two schemes diverge when using the same larger time step size.

Projected IMF results

In this section, we apply the projected IMF to locate the saddle points of the Ginzburg-Landau free energy in the H^{-1} metric. The second minimization subproblem in the IMF is solved by evolving the gradient flow:

$$\frac{\partial\phi}{\partial t} = -\mathbf{P}\Big[-\kappa^2\Delta\phi + (\phi^3-\phi)\Big] + 2\left\langle v, -\kappa^2\Delta\hat{\phi} + (\hat{\phi}^3-\hat{\phi})\right\rangle_{L^2}\mathbf{P}v. \tag{4.56}$$

TABLE 4.6 Comparisons of gradient descent method, semi-implicit scheme and SAV for the subproblem $\operatorname{argmin}_\phi L(\phi;\phi^{(0)},v^{(1)})$ in the IMF. The integers represent the number of iterations to attain the tolerances $\|\Delta\delta_\phi L\|_{H^{-1}} \le 10^{-4}$ or 10^{-6} using various step sizes Δt.

Δt	The number of iterations					
	$\|\Delta\delta_\phi L\|_{H^{-1}} \le 10^{-4}$			$\|\Delta\delta_\phi L\|_{H^{-1}} \le 10^{-6}$		
	IMF-GD	IMF-SI	IMF-SAV	IMF-GD	IMF-SI	IMF-SAV
1e-4	5276	5118	5162	6067	5911	6011
1e-3	∞	966	986	∞	1298	1263
1e-2	∞	∞	269	∞	∞	350
1e-1	∞	∞	206	∞	∞	256

TABLE 4.7 Comparison of the number of outer cycles required for IMF-GD, IMF-SI, and IMF-SAV when achieving the tolerance $\|\Delta\delta_\phi F\|_{H^{-1}} \le 10^{-8}$ by using various time step sizes Δt and fixed inner iterations numbers.

Δt	The number of cycles					
	iter# = 50			iter# = 100		
	IMF-GD	IMF-SI	IMF-SAV	IMF-GD	IMF-SI	IMF-SAV
1e-4	101	96	98	61	56	59
1e-3	∞	33	32	∞	17	18
1e-2	∞	∞	12	∞	∞	8
1e-1	∞	∞	11	∞	∞	7

To discretize the dynamics, we apply the convex splitting technique, which leads to the following time-discrete scheme:

$$\begin{aligned}\frac{\phi^{n+1}-\phi^n}{\Delta t} =& \mathbf{P}\left[\kappa^2\Delta\phi - 2\phi - 2\langle v,\phi\rangle v\right]^{n+1} \\ &+\mathbf{P}\left[-\phi^3+3\phi+2\left\langle v,-\kappa^2\Delta\hat{\phi}+\hat{\phi}^3\right\rangle v\right]^n.\end{aligned} \tag{4.57}$$

In the simulation, we set $\kappa = 0.04$, with the mesh grid $\{x_i = ih, i = 0,1,2,\ldots,N\}$, where $h = 1/N$, $N = 100$, and $\Delta t = 0.1$. We test both the projected IMF and the projected GAD under periodic boundary conditions and find that both methods yield the same transition state. Fig. 4.9**a** shows the saddle point of $F(\phi)$ in the H^{-1} metric [37], which matches the result obtained by applying the IMF directly in the H^{-1} metric. Additionally, the quadratic convergence rate is verified for the projected IMF, as shown in Fig. 4.9**b**. To demonstrate the efficiency of this method, we compare the CPU time required for the original IMF in the H^{-1} metric with the projected IMF, both using the same number of inner iterations. Table 4.8 presents the comparison results for various initial states, ϕ_{01}, ϕ_{02} and ϕ_{03}. The results indicate that the projected method reduces computational cost by nearly half, particularly when large inner iteration numbers are used.

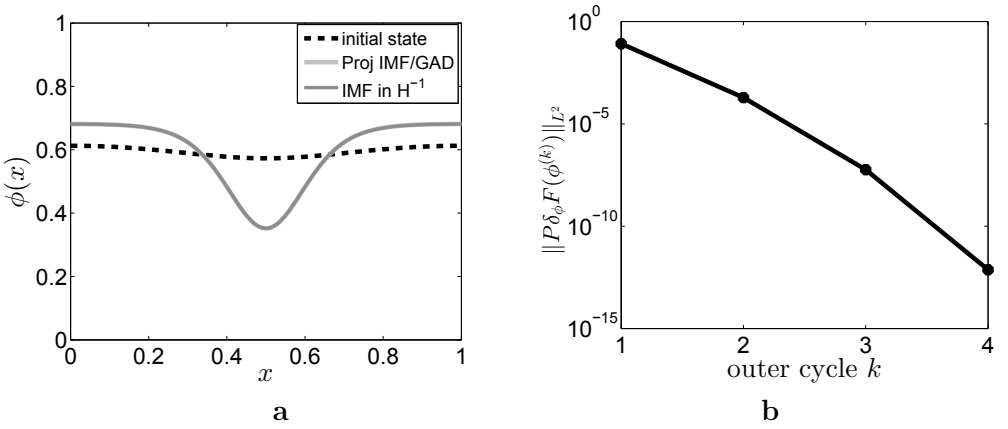

Figure 4.9 **a**: Initial state (dashed line); transition state by projected IMF or projected GAD (light grey line); transition state by IMF in H^{-1} metric (dark grey line). **b**: The decay of the error $\|\mathbf{P}\delta_\phi F(\phi^{(k)})\|_{L^2}$ measured by the L^2 norm of the projected force at each cycle k.

projected IPM results

In the previous subsection, the transition state of the Ginzburg-Landau free energy in the H^{-1} metric was obtained using the projected IMF. This method reduces the fourth-order spatial derivatives to second-order derivatives, resulting in a computational cost savings of approximately half. However, in practice, the initial state is typically chosen from the MEP, which lies within the domain of the saddle point. This assumption may not always hold, and the initial condition can be arbitrary. If the initial state is far from the saddle point, or even within the domain of a local minimum, the IMF can diverge when the number of inner iterations is large. Therefor, the convergence of the IMF method is highly dependent on both a good initial guess and the number of inner iterations M. To address this issue, we apply the IPM method combined with the projected technique to locate the saddle point of the Ginzburg-Landau free energy in the H^{-1} metric. In the IPM framework,

TABLE 4.8 CPU time (seconds) comparison. "IMF" means the original IMF in H^{-1} metric; "Projected IMF" is in L^2 metric.

	iter#	$1e4$	$2e4$	$5e4$	$1e5$	$2e5$
ϕ_{01}	IMF	16.11	32.06	80.52	158.75	320.99
	Projected IMF	9.14	18.14	45.94	91.07	182.68
ϕ_{02}	IMF	15.73	32.42	80.55	158.87	316.28
	Projected IMF	9.30	18.26	45.27	90.75	179.99
ϕ_{03}	IMF	16.02	33.21	80.24	160.02	325.60
	Projected IMF	9.17	18.43	45.71	91.13	183.00

we use the quartic form described in Remark 4.5, and the auxiliary functional becomes

$$L_\rho(\phi, \phi^l) = \int_\Omega \left[\frac{\kappa^2}{2} |\nabla \phi|^2 + f(\phi) - \kappa^2 |\nabla \hat{\phi}|^2 - 2f(\hat{\phi}) \right] dx + \rho \int_\Omega |\phi - \phi^l|^4 \, dx. \tag{4.58}$$

The gradient flow of the auxiliary functional $L_\rho(\phi, \phi^l)$ in the H^{-1} metric is governed by the equation

$$\frac{\partial \phi}{\partial t} = \Delta \delta_\phi L_\rho(\phi),$$

where

$$\delta_\phi L_\rho(\phi) = -\kappa^2 \Delta \phi + (\phi^3 - \phi) + 2 \left\langle v_1, \kappa^2 \Delta \hat{\phi} - (\hat{\phi}^3 - \hat{\phi}) \right\rangle_{L^2} v_1 + 4\rho(\phi - \phi^l)^3,$$

and $\hat{\phi} = \phi^l + \left\langle v_1, \phi - \phi^l \right\rangle_{H^{-1}} v_1$.

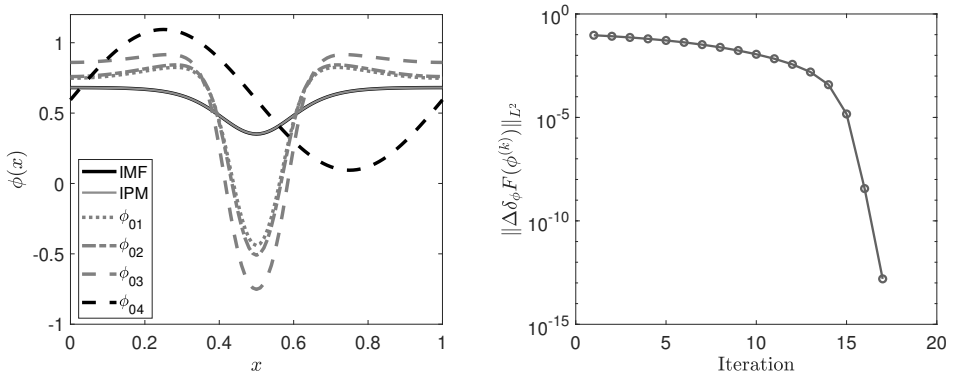

a **b**

Figure 4.10 **a**: Transition state (solid curves) computed using the IMF and IPM, starting from different initial states. The dashed curves represent the initial states from the minimum energy path (MEP) as listed in Table 4.9. The dark dashed curve corresponds to the initial state $\phi_{04} = 0.5\sin(2\pi x)+0.6$. **b**: Decay of the error $\|\Delta\delta_\phi F(\phi^l)\|_{L^2}$ measured by the L^2- norm of the $H^{-1}-$gradient, starting from the initial state ϕ_{01} with $\rho = 100$ and $M = 1000$.

In the numerical simulation, we use a uniform mesh grid for spatial discretization: $\{x_i = ih, i = 0, 1, 2, \ldots, N\}$, with $h = 1/N$ and $N = 100$. The time step is set as $\Delta t = 0.1$, and the periodic boundary conditions are applied. For the IPM method, we set the penalty parameter $\rho = 100$. The saddle point of $F(\phi)$ is obtained using this approach is shown in Fig. 4.10 **a**, and it matches the results reported in [42, 37]. Moreover, the quadratic convergence rate of the IPM algorithm is empirically verified, as demonstrated in Fig. 4.10

TABLE 4.9 Comparison of numerical convergence for three differential initial guesses ϕ_{01}, ϕ_{02}, and ϕ_{03}, as shown in Fig. 4.10**a**. "IMF" refers to the original IMF ($\rho = 0$), while "IPM" denotes the method with $\rho = 100$. M is the number of gradient descent steps used in minimizing the auxiliary functions. The symbols "✓" and "✗" indicate convergence and divergence, respectively.

M	ϕ_{01}		ϕ_{02}		ϕ_{03}		ϕ_{04}	
	IMF	IPM	IMF	IPM	IMF	IPM	IMF	IPM
10	✓	✓	✓	✓	✓	✓	✓	✓
100	✓	✓	✓	✓	✗	✓	✓	✓
200	✓	✓	✗	✓	✗	✓	✗	✓
500	✗	✓	✗	✓	✗	✓	✗	✓

b. To illustrate the advantages of this method, we compare the convergence results of the original IMF ($\rho = 0$) and the IPM ($\rho = 100$) for different initial states and varying inner iteration numbers M. Table 4.9 presents the convergence/divergence outcomes for four initial states ϕ_{01} to ϕ_{04}, confirming that the introduction of the proximal penalty in the IPM significantly improves the stability and widens the range of M values for which convergence is achieved, as compared to the original IMF.

Additionally, the IPM method is applied to locate the saddle point of the Ginzburg-Landau free energy in L^2 metric. The auxiliary functional L_ρ is the same as that in (4.58). The gradient flow of $L_\rho(\phi, \phi^l)$ in the L^2 metric is given by:

$$\frac{\partial \phi}{\partial t} = -\delta_\phi L_\rho(\phi) = \kappa^2 \Delta\phi - (\phi^3 - \phi) - 2\left\langle v_1, \kappa^2 \Delta\hat{\phi} - (\hat{\phi}^3 - \hat{\phi})\right\rangle_{L^2} v_1 - 4\rho(\phi - \phi^l)^3,$$

with $\hat{\phi} = \phi^l + \left\langle v_1, \phi - \phi^l \right\rangle_{L^2} v_1$.

In the numerical tests, we set $\kappa = 0.1$ and apply periodic boundary conditions. Fig. 4.11a shows the transition state (solid line) of the Allen-Cahn equation and the initial condition (dashed line) used in all tests. The remaining four figures illustrate the decay of the error, measured by $\|\delta_\phi F(\phi^l)\|_{L^2}$, in various settings, as a function of the number of the outer cycles (denoted as "Iteration" in the figures, which corresponds to the iteration index t in Algorithm 1.) Through extensive testing with various values of ρ and M, we observe that when $\rho = 0$ or is too small, the algorithm is prone to divergence as the inner iteration number M increases. However, By increasing ρ, we expand the valid range for M in which the algorithm converges. For example, when $\rho = 0.3$, M can be as large as 1272 and still result in successful convergence (Fig. 4.11c), while for $\rho = 1$, this range can extend up to 10^4 (Fig. 4.11d). In contrast, with $\rho = 0$, the valid range for M is limited to $[1, 450]$ (Fig. 4.11e).

We also explore the efficiency by measuring the error decay in terms of total computational cost. Table 4.10 suggests that the efficiency is not significantly affected by the inner iteration M. However, the value of ρ can have a

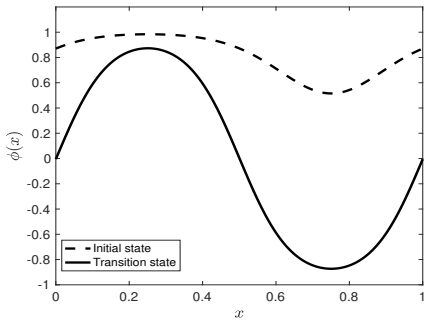

a Transition state

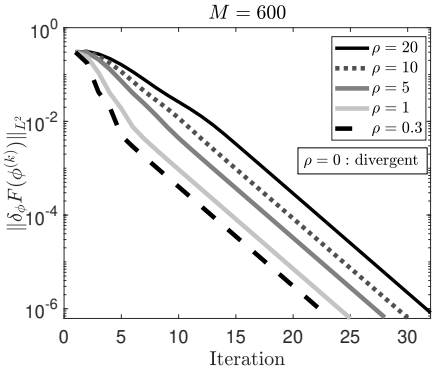

b $M = 600$

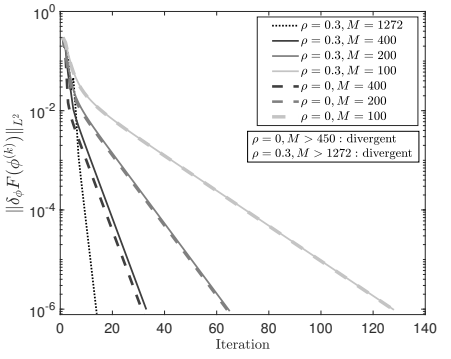

c Error decay

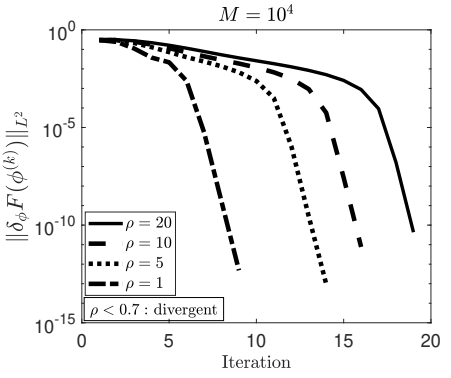

d $M = 10^4$

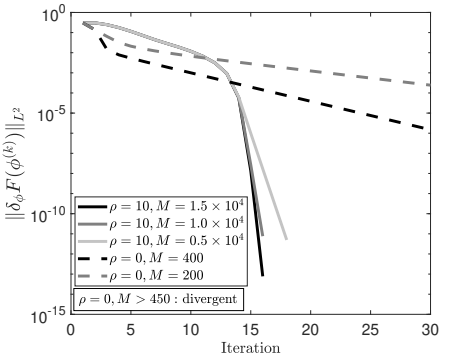

e Error decay

Figure 4.11 **a:** Transition state (solid curves) and the initial state (dashed line); **b:** Error decay, measured by $\|\delta_\phi F(\phi^l)\|_{L^2}$, with respect to the outer cycles for a fixed inner iteration number $M = 600$ and various $\rho = 0.3, 1, 5, 10, 20$. **c:** Error decay with respect to the outer cycles for $\rho = 0.3$ (solid lines) and $\rho = 0$ (dashed lines), using different inner iteration numbers $M = 100, 200, 400$, and 1272. The case for $M > 450$ with $\rho = 0$ diverges. **d:** Error decay with respect to the outer cycles for $M = 10^4$ and various values of $\rho = 1, 5, 10, 20$: **e:** Error decay with respect to the outer cycles for $\rho = 10$ (solid lines) and $\rho = 0$ (dashed lines), using different inner iteration numbers $M = 0.5 \times 10^4, 1.0 \times 10^4$, and 1.5×10^4. The case for $M > 450$ with $\rho = 0$ diverges.

Table 4.10 Effect of the inner iteration number M: **a** and **b** show the required number of outer cycles ($Iter$) and the total computational cost (calculated as the product of M and $Iter$) for different inner iteration numbers $M = 100, 200, 400$, when the error reaches 10^{-6}. The results are presented for two values of the penalty parameter $\rho = 0$ and $\rho = 0.3$, respectively. As the inner iteration number M increases, the required number of outer cycles decreases, while the total cost remains almost constant.

M	Iter	Total Cost
100	128	12800
200	64	12800
400	32	12800

a $\rho = 0$

M	Iter	Total Cost
100	127	12700
200	64	12800
400	32	12800

b $\rho = 0.3$

substantial impact. Fig. 4.11b (with $M = 600$) and Fig. 4.11d (with $M = 10^4$) show that smaller values of ρ lead to better error decay, especially for very large M. These empirical findings suggest a trade off between robustness and efficiency: robustness typically requires a large ρ, while efficiency benefits from a small ρ. Therefore, the optimal value of ρ must be fine-tuned to strike a balance between these two factors.

4.5.2 Landau-Brazovskii Free Energy

In this section, we expore the nucleation problem of phase transition in diblockcopolymers [68, 100]. The model is described by the Landau-Brazovskii energy functional for the order parameter ϕ, given by

$$F(\phi) = \int_\Omega \frac{\xi^2}{2}[(\Delta + 1)\phi(\mathbf{r})]^2 + \Phi(\phi)\ \mathrm{d}\,\mathbf{r}, \tag{4.59}$$

where the potential $\Phi(\phi)$ is defined as

$$\Phi(\phi) = \frac{\tau}{2}\phi^2 - \frac{\gamma}{3!}\phi^3 + \frac{1}{4!}\phi^4.$$

Here, the parameters are set to $\tau = -0.15, \xi = 1.0$, and $\gamma = 0.25$. We consider the two-dimensional domain $\Omega = [0, L_x] \times [0, L_y]$ with periodic boundary conditions. The two metastable states under consideration are the lamellar phase and the cylindrical phase. Additionally, we are interested in the transition state of $F(\phi)$ in the H^{-1} metric, which ensures mass conservation: $\int_\Omega \phi(\mathbf{r})\mathrm{d}\mathbf{r} = 0$.

The first and second order variations of $F(\phi)$ in the L^2 metric are computed as follows:

$$\delta_\phi F(\phi) = \xi^2(\Delta + 1)^2\phi(\mathbf{r}) + \Phi'(\phi),$$
$$\delta_\phi^2 F(\phi) = \xi^2(\Delta + 1)^2 + \Phi''(\phi) := \mathbf{H},$$

where $\Phi'(\phi) = \tau\phi - \frac{\gamma}{2}\phi^2 + \frac{1}{3!}\phi^3$, $\Phi''(\phi) = \tau - \gamma\phi + \frac{1}{2}\phi^2$, and $\widehat{\mathbf{H}} = \mathbf{PHP}$.

In the IMF approach, the eigenvector problem reads

$$\begin{cases} \widetilde{\mathbf{H}}(\phi)\psi = -\Delta\Big[\xi^2(\Delta+1)^2 + \Phi''(\phi)\Big]\psi = \lambda\psi, \\ \quad \int_\Omega \psi(\mathbf{r})\mathrm{d}\mathbf{r} = 0. \end{cases}$$

Here, the eigenvector v corresponds to the smallest eigenvalue of $\widetilde{\mathbf{H}}$. The gradient flow associated with the minimization subproblem for the functional $L(\phi;\phi^{(k)},v^{(k+1)}) = F(\phi) - 2F(\hat{\phi})$ is:

$$\frac{\partial\phi}{\partial t} = \Delta\frac{\delta L}{\delta\phi} = \xi^2\Delta(\Delta+1)^2\phi + \Delta\Phi_1(\phi) + 2\left\langle v, \xi^2(\Delta+1)^2\hat{\phi} + \Phi_1(\hat{\phi})\right\rangle_{L^2} v, \tag{4.60}$$

where $\Phi_1(\phi) = \Phi'(\phi) = \tau\phi - \gamma\phi^2/2! + \phi^3/3!$ and $\hat{\phi}$ is defined as in (4.47).

Convex splitting method results

Convex-splitting scheme. Two convex splitting forms of the Landau-Brazovskii energy functional $F(\phi)$ are chosen as $F(\phi) = F_c^{\mathrm{l}}(\phi) - F_e^{\mathrm{n}}(\phi)$, with

$$F_c^{\mathrm{l}}(\phi) = \int_\Omega \frac{\xi^2}{2}\Big[(\Delta+1)\phi\Big]^2 + \frac{\tau+22.75}{2}\phi^2\, d\mathbf{r}, \tag{4.61}$$

$$F_e^{\mathrm{n}}(\phi) = \int_\Omega \Big[-\frac{1}{4!}\phi^4 + \frac{\gamma}{3!}\phi^3 + \frac{22.75}{2}\phi^2\Big]\, d\mathbf{r}, \tag{4.62}$$

and $F(\phi) = \widetilde{F}_c^{\mathrm{n}}(\phi) - \widetilde{F}_e^{\mathrm{l}}(\phi)$, with

$$\widetilde{F}_c^{\mathrm{n}}(\phi) = \int_\Omega \frac{\xi^2}{2}|\Delta\phi|^2 + (\frac{1}{4!}\phi^4 - \frac{\gamma}{3!}\phi^3 + \frac{\xi^2+\tau}{2}\phi^2)\, d\mathbf{r}, \tag{4.63}$$

$$\widetilde{F}_e^{\mathrm{l}}(\phi) = \int_\Omega \xi^2|\nabla\phi|^2\, d\mathbf{r}. \tag{4.64}$$

By substituting (4.61), (4.62), (4.63), and (4.64) into the expressions

$$L_c(\phi) = F_c^{\mathrm{l}}(\phi) + 2\widetilde{F}_e^{\mathrm{l}}(\hat{\phi}) \quad \text{and} \quad L_e(\phi) = F_e^{\mathrm{n}}(\phi) + 2\widetilde{F}_c^{\mathrm{n}}(\hat{\phi}),$$

we obtain the convex splitting form for $L(\phi) = L_c(\phi) - L_e(\phi)$, leading to the discrete scheme:

$$\frac{\phi^{n+1}-\phi^n}{\Delta t} = \Delta[\delta_\phi L_c(\phi)]^{n+1} - \Delta[\delta_\phi L_e(\phi)]^n.$$

This gives the equation:

$$\begin{aligned} \frac{\phi^{n+1}-\phi^n}{\Delta t} =& \Big[\xi^2\Delta(\Delta+1)^2\phi + (\tau+22.75)\Delta\phi\Big]^{n+1} + 4\xi^2\Big[\langle\Delta v, v\rangle\langle w,\phi\rangle v\Big]^{n+1} \\ &+ 4\xi^2\Big[\Big\langle\Delta\phi^{(k)}, v\Big\rangle - \Big\langle w, \phi^{(k)}\Big\rangle\langle\Delta v, v\rangle\Big]v - \Delta\Big[-\frac{1}{3!}\phi^3 + \frac{\gamma}{2}\phi^2 + 22.75\phi\Big]^n \\ &+ 2\Big[\Big\langle v, \xi^2\Delta^2\hat{\phi} + (\xi^2+\tau)\hat{\phi} - \frac{\gamma}{2}\hat{\phi}^2 + \frac{1}{3!}\hat{\phi}^3\Big\rangle v\Big]^n, \end{aligned} \tag{4.65}$$

where $\langle\cdot,\cdot\rangle$ denotes the inner product in the L^2 space.

Remark 4.9 *The convex splitting forms in* (4.61)*,* (4.63) *and* (4.64) *are globally convex. For the form in* (4.62)*, the constant* C *in Remark 4.8 is taken as* 22.75*, which ensures that the convex region is* $[-6.5, 6.5]$*. This interval precisely spans the range of the initial guess. Additionally, we observe that the values of* ϕ *consistently remain within the interval* $[-6.5, 6.5]$ *throughout the numerical simulation.*

For the numerical test, the domain is $\Omega = [0, \frac{16}{\sqrt{3}}\pi] \times [0, 8\pi]$, and the mesh girds are $\{x_i = ih_x, i = 0, 1, 2, \ldots, N_x.\}$ and $\{y_j = jh_y, j = 0, 1, 2, \ldots, N_y\}$, with $h_x = 1/N_x, h_y = 1/N_y$, and $N_x = N_y = 100$. To locate the steady states of $F(\phi)$, We first consider the gradient flow $\partial_t\phi = \Delta\delta_\phi F = \Delta[\xi^2(\Delta + 1)^2\phi + \Phi_1(\phi)]$. The initial conditions are taken from equation (2.21) in [100]. The convex splitting method, based on the forms in (4.61) and (4.62), is applied to construct the numerical scheme. The steady states, including the lamellar phase and the cylindrical phase, are shown in Fig. 4.12**a** and 4.12**c**, respectively. The transition state obtained using the IMF method is shown in Fig. 4.12**b** [42].

Scalar auxiliary variable results

To implement the second-order numerical scheme described in equation (4.22), the operator $\mathcal{L}$ and the energy L_n are defined as:

$$\mathcal{L} = \xi^2(\Delta + 1)^2, \qquad L_n = \int_\Omega \Phi(\phi) + \frac{\xi^2}{2}[(\Delta + 1)\hat{\phi}]^2 + \Phi(\hat{\phi})\ \mathrm{d}\mathbf{x}.$$

Next, we compute the derivative of $L_n(\phi)$ with respect to ϕ:

$$\frac{\delta L_n(\phi)}{\delta\phi} = \Phi'(\phi) - 2v\left\langle w, \xi^2(\Delta + 1)^2\hat{\phi} + \Phi'(\hat{\phi})\right\rangle_{L^2}.$$

We now present the results for two-dimensional and three-dimensional cases, respectively.

2D domain case. For the two-dimensional case, we investigate three different domain sizes: small, medium, and large.

- Small domain: For the domain $\Omega = [0, \frac{16\pi}{\sqrt{3}}] \times [0, 8\pi]$, the mesh size is $N_x = N_y = 60$. Fig. 4.13**a** and 4.13**b** show the two stable stationary states: the lamellar phase and the cylindrical phase. Fig. 4.13**c** presents the transition state obtained using the IMF-SAV method, which aligns closely with the result in Fig. 4.12**b** by the convex splitting method. The quadratic convergence rate is validated and shown in Fig. 4.13**d**. These result have been published in [39].

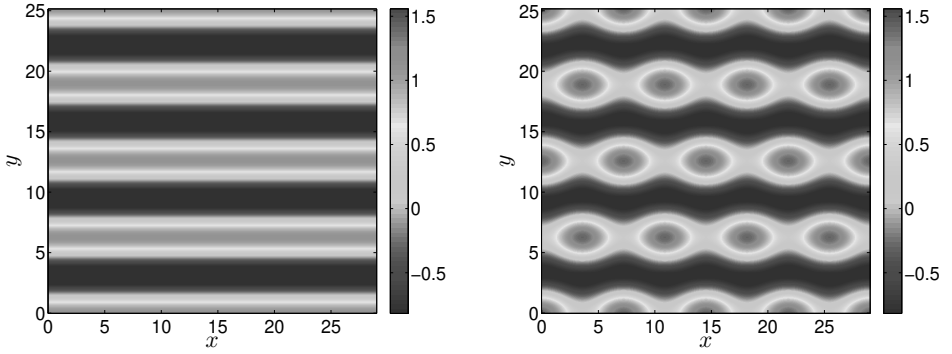

a lamellar phase

b Transition state

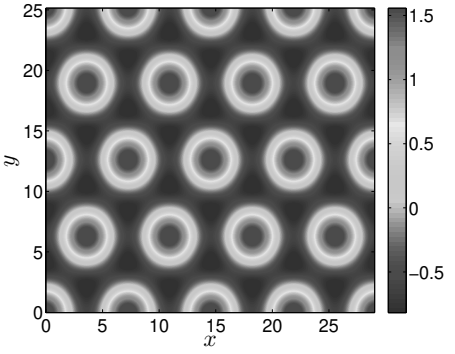

c cylindrical phase

Figure 4.12 Two stable stationary states **a** and **c** and the transition state **b** of the 2-D Landau-Brazovskii energy in the H^{-1} metric. Their corresponding free energies are -16.486, -16.447, and -17.290, from left to right. The smallest eigenvalues are 3.50×10^{-6}, -4.32×10^{-6}, and 3.32×10^{-6}, respectively.

- Medium domain: For the domain $[0, \frac{32\pi}{\sqrt{3}}] \times [0, 16\pi]$, with $N_x = N_y = 240$. The results are shown in Fig. 4.14 [39].
- Large domain: The domain is $\Omega = [0, \frac{64\pi}{\sqrt{3}}] \times [0, 32\pi]$, with $N_x = N_y = 960$. The corresponding results are presented in Fig. 4.15 [39].

In all three cases, the transition states display the critical nucleus features at various computational sizes. We observe that as the domain size increases, nucleation becomes more pronounced and occurs near the centre of the domain, consistent with findings in [68]. Furthermore, the region where nucleation appears to have a fixed physical size, regardless of the computational domain's size.

3D domain case In this subsection, we investigate the transition states of the Landau-Brazovskii free energy on a three-dimensional domain $\Omega =$

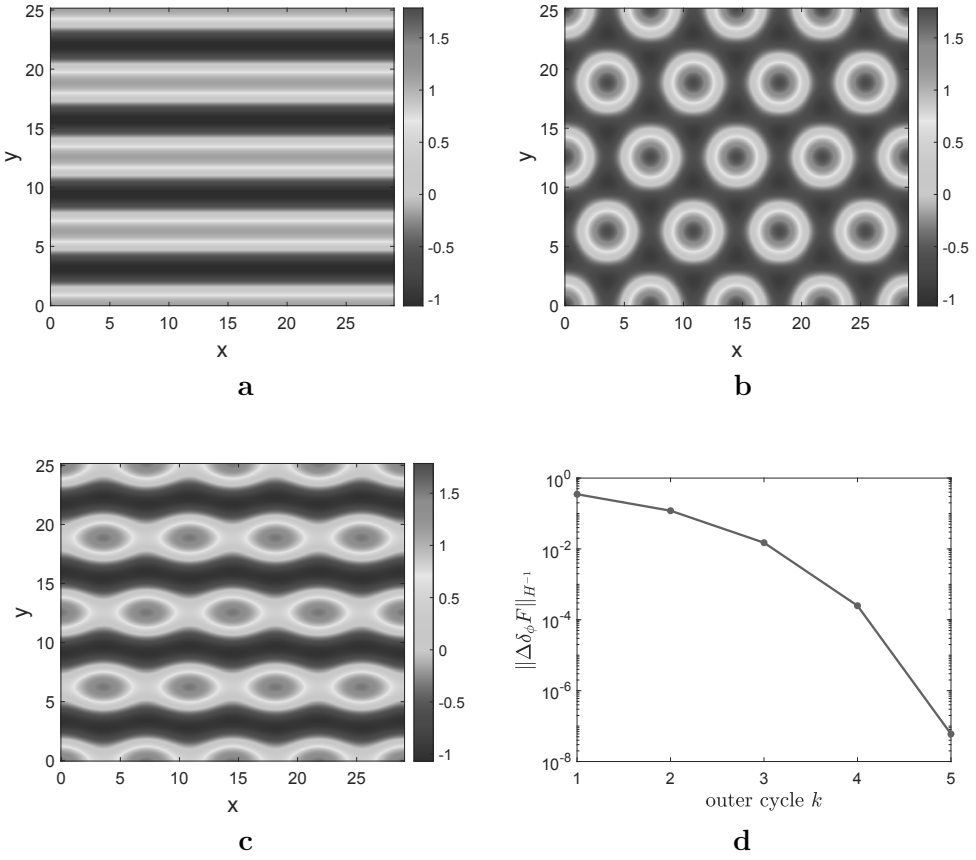

Figure 4.13 Small domain $\Omega = [0, \frac{16\pi}{\sqrt{3}}] \times [0, 8\pi]$: **a** and **b** are two stable stationary states of the Landau-Brazovskii free energy in the H^{-1} metric; **c** is the transition state; **d** shows the decay of the error $\|\Delta\delta_\phi F\|_{H^{-1}}$ (measured by the H^{-1} norm of the force) in each cycle k.

$[0, \frac{16\pi}{\sqrt{3}}] \times [0, 8\pi] \times [0, \pi]$, with the mesh sizes $N_x = N_y = 60$ and $N_z = 8$. The transition state obtained using the IMF-SAV method is shown in Fig. 4.16**c**, Fig. 4.16**a** and Fig. 4.16**b** are two steady states [39]. This transition state exhibits a similar structure to the two-dimensional case, but it is extended in the $z-$direction. Its projection onto the $xy-$plane corresponds exactly to the two-dimensional transition state presented in Fig. 4.13**c**. Furthermore, Fig. 4.17 illustrates the quadratic convergence rate of the IMF-SAV method in this three-dimensional setting [39]. Given that the free energy landscape is significantly more complex in three dimensions, it is possible that there are additional transition states that are not captured by our numerical results. These potential states remain an area for future research and exploration.

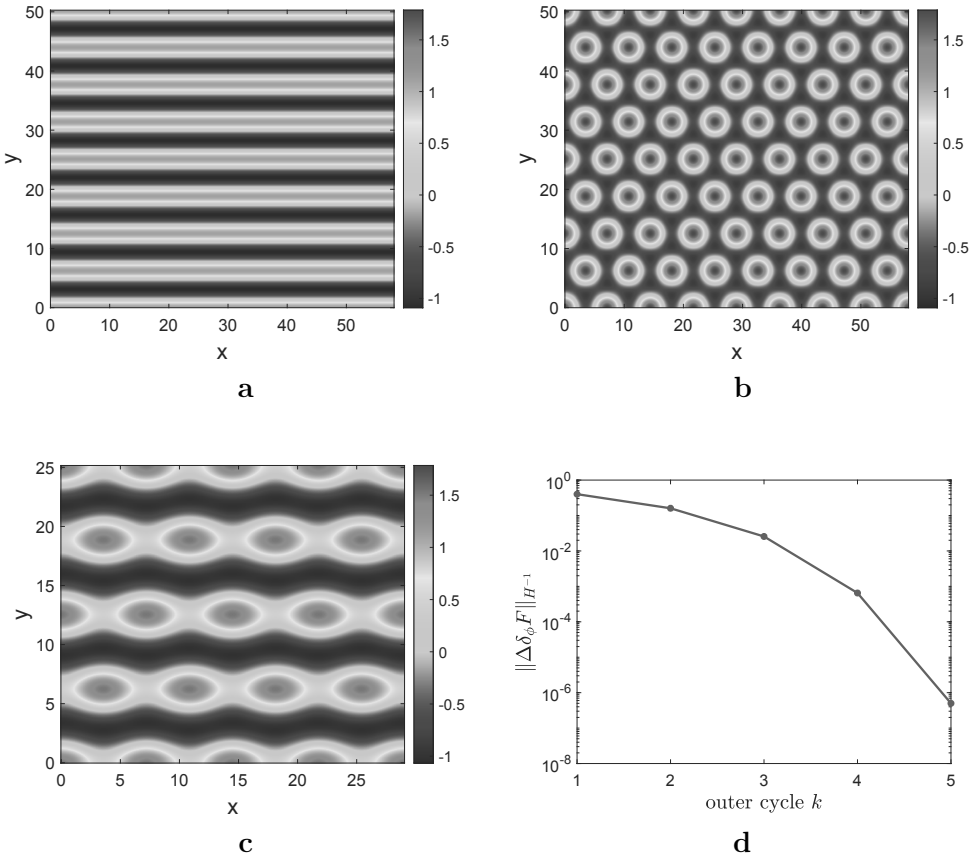

Figure 4.14 Medium domain $\Omega = [0, \frac{32\pi}{\sqrt{3}}] \times [0, 16\pi]$: **a** and **b** are two stable stationary states of the Landau-Brazovskii free energy; **c** is the transition state obtained; **d** shows the decay of the error $\|\Delta\delta_\phi F\|_{H^{-1}}$ (measured by the H^{-1} norm of the force) in each cycle k.

projected IMF results

In this section, we compute the transition state of the Landau-Brazovskii (LB) free energy in the H^{-1} metric, using the projected IMF. The second minimization subproblem in the IMF is transformed into the gradient flow:

$$\frac{\partial \phi}{\partial t} = -\mathbf{P}\Big[\xi^2(\Delta+1)^2\phi + \Phi'(\phi)\Big] + 2\left\langle v, \xi^2(\Delta+1)^2\hat{\phi} + \Phi'(\hat{\phi})\right\rangle_{L^2}\mathbf{P}v,$$

where the parameter ξ remains the same as in previous calculations.

For the two-dimensional numerical example, we assume the periodic boundary conditions. Since this is a fourth-order equation in space, we employ the Fast Fourier Transform (FFT) to reduce computational cost. We use a mesh size of $Nx = Ny = 64$ and a time step size of $\Delta t = 0.1$. The transition state calculated by the projected IMF (or projected GAD) is shown in Fig.

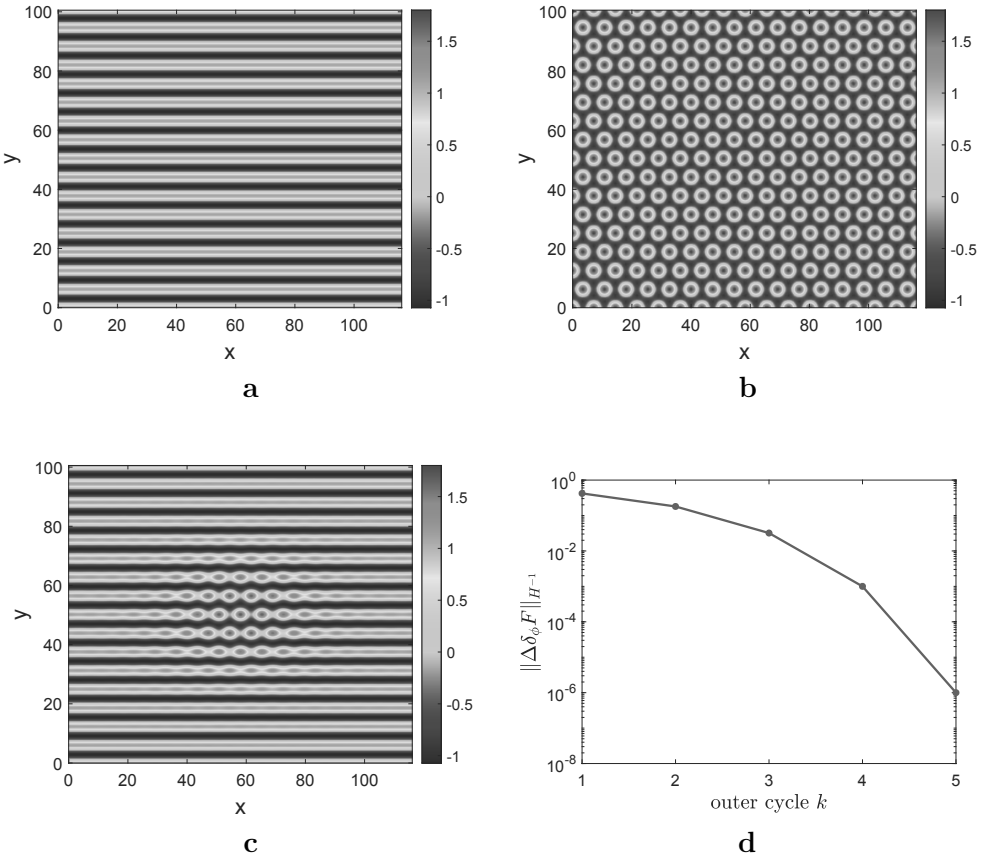

Figure 4.15 Large domain $\Omega = [0, \frac{64\pi}{\sqrt{3}}] \times [0, 32\pi]$: **a** and **b** are two stable stationary states of the Landau-Brazovskii free energy; **c** is the transition state obtained; **d** shows the decay of the error $\|\Delta\delta_\phi F\|_{H^{-1}}$ (measured by the H^{-1} norm of the force) in each cycle k.

4.18**a** [37], which matches the result obtained by the IMF in the H^{-1} metric directly (Fig. 4.12**b**). Fig. 4.18**b** shows the quadratic convergence rate of the projected IMF [37]. Additionally, we compare the computational efficiency of the projected IMF with the original IMF in the H^{-1} metric. The comparison is based on the CPU time required for each method, with the same inner iteration number for both methods. We test various iteration counts: iter# $= 5 \times 10^3, 6 \times 10^3, 7 \times 10^3, 8 \times 10^3, 9 \times 10^3$ and 10^4. The results, shown in Table 4.11, indicate that the projected IMF method saves approximately one-third of the computational cost compared to the original IMF.

In conclusion, we have explored various advanced strategies for improving the Iterative Minimization Formulation (IMF) in the context of saddle point identification. The focus was on efficiently solving the translation step by reformulating the problem into a gradient flow dynamics framework and

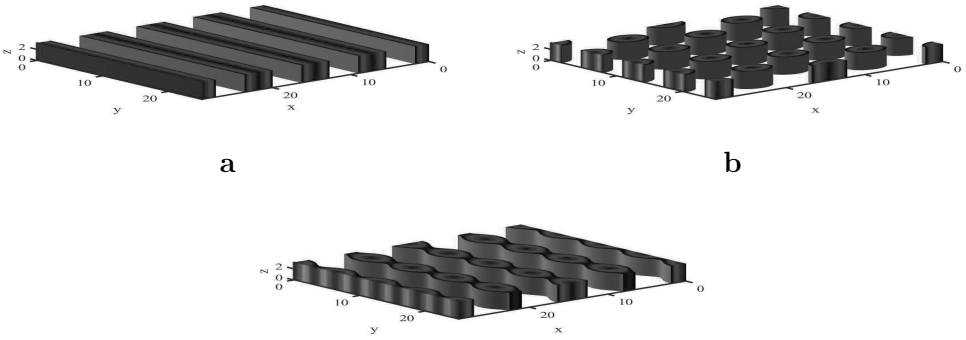

Figure 4.16 3D domain $\Omega = [0, \frac{16\pi}{\sqrt{3}}] \times [0, 8\pi] \times [0, \pi]$: **a** and **b** are two steady states of the Landau-Brazovskii free energy; **c** presents the transition state.

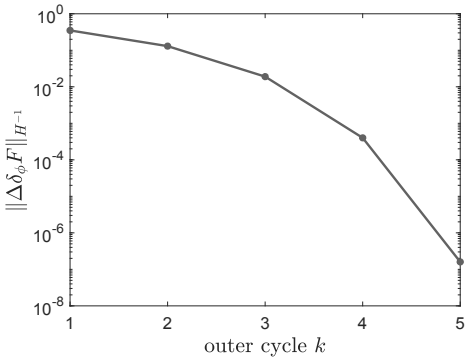

Figure 4.17 Decay of the error $\|\Delta\delta_\phi F\|_{H^{-1}}$, measured by the H^{-1} norm of the force in each cycle k.

TABLE 4.11 CPU time (seconds) comparison. "IMF" refers to the original IMF in the H^{-1} metric, and "Projected IMF" is in L^2 metric.

	iter #	$5e3$	$6e3$	$7e3$	$8e3$	$9e3$	$1e4$
ϕ_{01}	IMF	12.62	15.27	17.67	20.35	22.71	25.84
	Projected IMF	9.03	11.05	12.71	14.07	16.06	17.62
ϕ_{02}	IMF	12.71	15.56	17.93	20.67	22.97	25.32
	Projected IMF	9.05	10.71	12.67	14.47	16.34	17.76
ϕ_{03}	IMF	12.77	15. 82	17.39	19.90	22.01	25.51
	Projected IMF	9.07	11.15	12.95	14.56	16.19	18.07

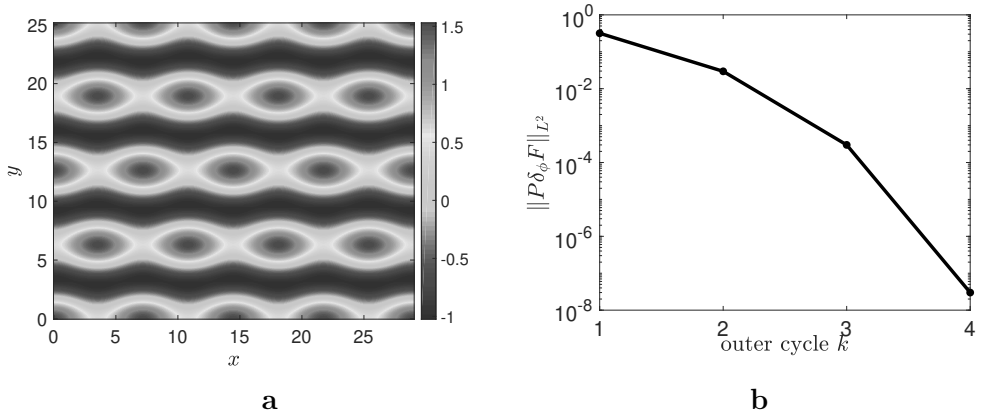

Figure 4.18 **a**: Transition state of the Landau Brazovskii free energy in the H^{-1} metric using the projected IMF. **b**: Decay of the error $\|\mathbf{P}\delta_\phi F(\phi^{(k)})\|_{L^2}$, measured by the L^2 norm of the projected force at each cycle k.

employing numerical techniques such as the convex splitting method and the Scalar Auxiliary Variable (SAV) approach. These methods allow for larger time step sizes, significantly improving computational efficiency. Additionally, a projection-based adaptation of IMF for the H^{-1} metric was introduced, addressing the challenges of saddle point calculations in this more complex metric. This adaptation, using a linear projection operator, reduces computational costs while maintaining accuracy. To further enhance the robustness of the IMF, we developed the Iterative Proximal Minimization (IPM) method. This method guarantees global convergence by incorporating a proximal function to ensure the strict convexity of the subproblems, enabling rapid convergence even with poor initial estimates. Collectively, the methods and innovations discussed in this chapter provide efficient, reliable, and scalable solutions for locating transition states, significantly advancing rare event studies and their applications in complex systems.

APPENDIX 1

The proof of Theorem 4.6

Proof Theorem 4.6 *To prove our conclusion, we will claim the optimization* (4.35) *is a strictly convex problem by showing that at a sufficiently large* ρ, L_ρ *is a strictly convex function of* y *in* $\mathbb{R}^d$ *uniformly for* $x \in \Omega_1'$. *This can be proved by showing that the minimal eigenvalues of the Hessian matrix are positive.*

The Hessian matrix of L_ρ with respect to y is

$$\begin{aligned} H_\rho(y;x) &:= \nabla_y^2 L_\rho(y;x,v_1(x)) \\ &= (1-\alpha)H(y) + \alpha\Big[\mathbf{I}-\Pi_1(x)\Big]H(y-\Pi_1(x)(y-x))\Big[\mathbf{I}-\Pi_1(x)\Big] \\ &\quad - \beta\Pi_1(x)\,H\left(x+\Pi_1(x)(y-x)\right)\Pi_1(x) + \rho\nabla_y^2 d(x,y) \\ &=: \mathcal{H}(y;x) + \rho\nabla_y^2 d(x,y), \end{aligned} \tag{4.66}$$

where $\Pi_1(x) := v_1(x)v_1(x)^\top$, and the new symmetric matrix

$$\begin{aligned} \mathcal{H}(y;x) := (1-\alpha)H(y) &+ \alpha\Big[\mathbf{I}-\Pi_1(x)\Big]H(y-\Pi_1(x)(y-x))\Big[\mathbf{I}-\Pi_1(x)\Big] \\ &- \beta\Pi_1(x)H(x+\Pi_1(x)(y-x))\Pi_1(x). \end{aligned} \tag{4.67}$$

By the inequality

$$\lambda_{\min}\left(H_\rho(y;x)\right) \geq \lambda_{\min}(\mathcal{H}(y;x)) + \rho\cdot\lambda_{\min}(\nabla_y^2 d(x,y)), \tag{4.68}$$

we focus on $\lambda_{\min}(\mathcal{H}(y;x))$ first.

Given a compact set Ω_1' in the index-1 region Ω_1, we first fix a point $x \in \Omega_1' \subset \Omega_1$. Then $\lambda_1(x) < 0 < \lambda_2(x)$. Note the eigenvectors of

$$\mathcal{H}(x;x) = (1-\alpha)H(x) + \alpha(\mathbf{I}-\Pi_1(x))H(x)(\mathbf{I}-\Pi_1(x)) - \beta\Pi_1(x)H(x)\Pi_1(x)$$

coincide with the eigenvectors of the Hessian matrix $H(x) = \nabla^2 V(x)$, because for $i \neq 1$, we have

$$\begin{aligned} \mathcal{H}(x;x)v_i(x) &= (1-\alpha)H(x)v_i(x) + \alpha(\mathbf{I}-\Pi_1(x))\lambda_i(x)v_i(x) + 0 \\ &= (1-\alpha)\lambda_i(x)v_i(x) + \alpha\lambda_i(x)v_i(x) \\ &= \lambda_i(x)v_i(x) \end{aligned}$$

and at $i = 1$,

$$\begin{aligned} \mathcal{H}(x;x)v_1(x) &= (1-\alpha)\lambda_1(x)v_1(x) + 0 - \beta\lambda_1(x)v_1(x) \\ &= (1-\alpha-\beta)\lambda_1(x)v_1(x). \end{aligned}$$

Therefore, the eigenvalues of $\mathcal{H}(x;x)$ are given by

$$\{(1-\alpha-\beta)\lambda_1(x), \lambda_2(x), \cdots, \lambda_d(x)\}$$

and they are all strictly positive since $\alpha+\beta > 1$ and $x \in \Omega_1$. Therefore $\mathcal{H}(x;x)$ is positive definite. In addition, since $V \in C^3(\mathbb{R}^d)$, for each x we have that $\lambda_{\min}(\mathcal{H}(y;x)) > 0$ for all y inside a ball neighbourhood $\mathcal{B}_{\varepsilon_x}(x)$ with a radius $\epsilon_x > 0$ depending on x, due to the continuity of $\nabla^2 V$. Specifically,

$$\epsilon_x := \frac{1}{2}\sup\{\epsilon > 0 : \min_{\|y-x\|\leq\epsilon} \lambda_{\min}(\mathcal{H}(y;x)) > 0\}$$

Pick up the smallest radius for all x in Ω_1':

$$\bar{\varepsilon} = \min_{x\in\Omega_1'} \epsilon_x > 0,$$

which is strictly positive since Ω_1' is compact. This means that

$$\inf_{x\in\Omega_1'} \inf_{\|y-x\|\le\bar{\epsilon}} \lambda_{\min}(\mathcal{H}(y;x)) > 0,$$

and then due to (4.68)*, for any $\rho \ge 0$, the Hessian matrix H_ρ satisfies the same condition*

$$\inf_{x\in\Omega_1'} \inf_{\|y-x\|\le\bar{\epsilon}} \lambda_{\min}(H_\rho(y;x)) > 0, \tag{4.69}$$

since $\nabla_y^2 d(x,y) \succeq 0$ due to **Assumption** *1a.*

In order to show $H_\rho(y;x) \succ 0$ for $y \in \mathbb{R}^d$, we choose a sufficiently large penalty factor ρ. By **Assumption** *1c, there exists a constant $\bar{\lambda}_{\bar{\varepsilon}} > 0$, such that $\lambda_{\min}(\nabla_y^2 d(x,y)) \ge \bar{\lambda}_{\bar{\varepsilon}}$ for any x, y satisfying $y \notin \mathcal{B}_{\bar{\varepsilon}}(x)$. Recall that from* **Assumption** *2c, the Hessian matrix of potential function V is bounded everywhere. Let $\bar{\lambda} = \max\{|\bar{\lambda}_L|, |\bar{\lambda}_U|\}$, then by noting* (4.67)*, we have the lower bound of the minimal eigenvalue for all $\|x-y\| \ge \bar{\varepsilon}$*

$$\begin{aligned}\lambda_{\min}\left(H_\rho(y;x)\right) &\ge \lambda_{\min}(\mathcal{H}(y;x)) + \rho\lambda_{\min}(\nabla_y^2 d(x,y)) \\ &\ge -(|1-\alpha| + |\alpha| + |\beta|)\bar{\lambda} + \rho\bar{\lambda}_{\bar{\epsilon}}.\end{aligned}$$

Let $\rho > \bar{\rho} := (1 + 2|\alpha| + |\beta|)\bar{\lambda}/\bar{\lambda}_{\bar{\varepsilon}} > 0$, then

$$\inf_{x\in\Omega_1'} \inf_{\|y-x\|>\bar{\epsilon}} \lambda_{\min}\left(H_\rho(y;x)\right) > 0.$$

Therefore, together with (4.69) *we conclude that when $\rho > \bar{\rho}$,*

$$\inf_{x\in\Omega_1'} \inf_{y\in\mathbb{R}} \lambda_{\min}\left(H_\rho(y;x)\right) > 0. \tag{4.70}$$

That is, $L_\rho(y;x,v_1(x))$ is strongly convex in y and the minimization problem in equation (4.35) *has a unique solution $\Phi_\rho(x)$ for all $x \in \Omega_1'$.*

Lastly, we show that for sufficiently large ρ, the unique solution

$$\hat{x} = \operatorname*{argmin}_{y\in\mathbb{R}^d} \left(L(y;x,v_1(x)) + \rho\cdot d(x,y)\right)$$

is in the index-1 region Ω_1 for any $x \in \Omega_1'$. It suffices to show that if ρ is large enough, then for any $x \in \Omega_1'$ and $y' \notin \Omega_1$, there exists $y \in \Omega_1$ such that

$$L(y;x,v_1(x)) + \rho\cdot d(x,y) < L(y';x,v_1(x)) + \rho\cdot d(x,y'). \tag{4.71}$$

The idea is to search for such a point y along the line segmentation between x and y'.

Let $\delta := \mathrm{dist}(\Omega_1', \partial\Omega_1)$ *be the distance between* Ω_1' *and the boundary of* Ω_1*, and assume that* $\delta = \mathrm{dist}(\Omega_1', \mathbb{R}^d \setminus \Omega_1)$*. Then* $\delta > 0$ *because* Ω_1 *is an open set and* Ω_1' *is a compact subset of* Ω_1*. We define the* $\delta/2$*-neighborhood of* Ω_1' *and its boundary:*

$$A_\delta := \{z : \mathrm{dist}(z, \Omega_1') \le \delta/2\} \subset \Omega_1 \text{ and } \partial A_\delta = \{z : \mathrm{dist}(z, \Omega_1') = \delta/2\}.$$

It is easy to show that $\mathrm{dist}(A_\delta, \partial\Omega_1) \ge \delta/2$*: There exist two points* $a_\delta^* \in \partial A_\delta$ *and* $b \in \partial\Omega_1$ *such that* $\mathrm{dist}(A_\delta, \partial\Omega_1) = \mathrm{dist}(\partial A_\delta, \partial\Omega_1) = \|a_\delta^* - b\|$*, and one point* $a^* \in \Omega_1'$ *such that* $\|a^* - a_\delta^*\| = \delta/2$ *since* $\mathrm{dist}(a_\delta^*, \partial\Omega_1) = \delta/2$*, then*

$$\mathrm{dist}(A_\delta, \partial\Omega_1) = \|a_\delta^* - b\| \ge \|a^* - b\| - \|a^* - a_\delta^*\| = \|a^* - b\| - \delta/2 \ge \delta/2.$$

Therefore, for any $y' \notin \Omega_1$ *and* $x \in \Omega_1'$*, we define* y *as an intersection point on the boundary* ∂A_δ *and the line segment between* y' *and* x *such that the line segment between* y *and* y' *are all outside of the* A_δ*. Since* $y \in \partial A_\delta$*,* $\|y - x\| \ge \mathrm{dis}(y, \Omega_1') = \delta/2$ *and* $\|y - y'\| \ge \mathrm{dist}(A_\delta, \partial\Omega_1) \ge \delta/2$*. Since the line segment* $y(t) = y + t(y' - y)$*,* $0 \le t \le 1$ *in outside of* A_δ*, we have* $\min_{t\in[0,1]} \|y(t) - x\| \ge \delta/2$*, which, by* **Assumption** *1c, gives that*

$$\min_{t\in[0,1]} \lambda_{\min}(\nabla_y^2 d(y(t), x) \ge \bar{\lambda}_{\frac{\delta}{2}} > 0$$

Therefore,

$$\begin{aligned} d(y', x) - d(y, x) &= \nabla_y d(y, x)^\top (y' - y) + \int_0^1 \int_0^t (y' - y)^\top \nabla_y^2 d(y(s), x)(y' - y) \mathrm{d}s\mathrm{d}t \\ &\ge \nabla_y d(y, x)^\top (y' - y) + \frac{1}{2}\bar{\lambda}_{\frac{\delta}{2}} \|y' - y\|^2 \\ &\ge \nabla_y d(y, x)^\top (y' - y) + \frac{1}{4}\delta\bar{\lambda}_{\frac{\delta}{2}} \|y' - y\|. \end{aligned} \tag{4.72}$$

In addition, by **Assumption** *1a and 1b about the convexity,* $0 = d(x, x) \ge d(y, x) + \nabla_y d(y, x)^\top (x - y)$*, which leads to* $\nabla_y d(y, x)^\top (y - x) \ge d(y, x) \ge 0$*, and*

$$\nabla_y d(y, x)^\top (y' - y) \ge 0, \tag{4.73}$$

as $y' - y$ *and* $y - x$ *are in the same direction. Therefore, by* (4.72) *we have shown that*

$$d(y', x) - d(y, x) \ge D_\delta \|y' - y\|,$$

where $D_\delta := \frac{1}{4}\delta\bar{\lambda}_{\frac{\delta}{2}}$*. Together with Lemma 4.1, we have*

$$\begin{aligned} L_\rho(y'; x, v_1(x)) &= L(y'; x, v_1(x)) + \rho \cdot d(y', x) \\ &\ge L(y; x, v_1(x)) - \mathrm{Lip}(L)\|y' - y\| + \rho\left(d(y', x) - d(y, x) + d(y, x)\right) \\ &\ge L(y; x, v_1(x)) + \rho \cdot d(y, x) + (\rho D_\delta - \mathrm{Lip}(L))\|y' - y\| \\ &= L_\rho(y; x, v_1(x)) + (\rho D_\delta - \mathrm{Lip}(L))\|y' - y\|. \end{aligned} \tag{4.74}$$

For any $\rho > \frac{\mathrm{Lip}(L)}{D_\delta}$, *we have*

$$L_\rho(y'; x, v_1(x)) > L_\rho(y; x, v_1(x)) \geq \min_{y\in\Omega_1} L_\rho(y; x, v_1(x)). \tag{4.75}$$

Then together with equation (4.70), *we have proved that the uniqueness of the global minimizer*

$$\hat{x} = \operatorname*{argmin}_{y\in\mathbb{R}^d} L_\rho(y; x, v_1(x))$$

and $\hat{x} \in \Omega_1$ *is within the index-1 region for any compact* $x \in \Omega_1' \subset \Omega_1$ *for sufficiently large*

$$\rho > \bar{\rho} := \max\left(\frac{\mathrm{Lip}(L)}{D_\delta}, \frac{(1+2|\alpha|+|\beta|)\bar{\lambda}}{\bar{\lambda}_{\bar{\varepsilon}}}\right).$$

Remark 4.10 $\bar{\rho}$ *depends on the uniform bound of Hessian* $\nabla^2 V$, *two constants* α, β, *and the compact subset* $\Omega_1' \subseteq \Omega_1$.

With results in Theorem 4.6, we are ready to present the proof of Theorem 4.5, which establishes the equivalence between the fixed points of the map $\Phi_\rho(\cdot)$ and the index-1 saddle points of the potential function $V(\cdot)$.

The proof of Theorem 4.5

Proof Theorem 4.5 *"Proof of Statement (1)":*
From Theorem 4.6, we know that for each index-1 saddle point $x_i^* \in \mathcal{S}_1$, *there exists a positive* $\bar{\rho}_i$ *such that* $L_\rho(y; x_i^*, v_1(x_i^*))$ *is a strictly convex function of* $y \in \mathbb{R}^d$ *for all* $\rho > \bar{\rho}_i$. *Together with* **Assumption** *2b and by setting* $\bar{\rho} := \max_i \bar{\rho}_i > 0$, *we have that for any* $x^* \in \mathcal{S}_1$, *then for any* $\rho > \bar{\rho}$, $L_\rho(y; x^*, v_1(x^*))$ *is a convex function of* $y \in \mathbb{R}^d$. *We only need to show that the first order condition holds. Note that*

$$\begin{aligned}\nabla_y L_\rho(y; x, v_1(x)) =& (1-\alpha)\nabla V(y) + \alpha(\mathbf{I}-\Pi_1)\nabla V(y - \Pi_1(y-x)) \\ &- \beta\Pi_1\nabla V(x + \Pi_1(y-x)) + \rho\nabla_y d(x,y),\end{aligned} \tag{4.76}$$

where $\Pi_1 = \Pi_1(x) = v_1(x)v_1(x)^\top$, *we get*

$$\nabla_y L_\rho(y; x, v_1(x))|_{y=x} = \Big[\mathbf{I} - (\alpha+\beta)\Pi_1(x)\Big]\nabla V(x)$$

by **Assumption** *1b. Thus,*

$$\nabla_y L_\rho(y; x^*, v_1(x^*))|_{y=x^*} = \mathbf{0}$$

thanks to $\nabla V(x^*) = \mathbf{0}$.

"Proof of Statement (2) ":
Now given that $\Phi_\rho(x^*) = \{x^*\}$, *i.e.,* x^* *is the unique minimizer in* (4.34),

we want to show x^* is an index-1 saddle point. This can be illustrated by showing that the first order condition $\nabla_y L_\rho(y; x^*, v_1(x^*))|_{y=x^*} = \mathbf{0}$ holds and the Hessian matrix $\nabla_y^2 L_\rho(y; x^*, v_1(x^*))|_{y=x^*}$ is positive semi-definite. By the first order condition, we have

$$\nabla L_\rho(y; x^*, v_1(x^*))|_{y=x^*} = \Big[\mathbf{I} - (\alpha+\beta)\Pi_1(x^*)\Big]\nabla V(x^*) = \mathbf{0}. \tag{4.77}$$

Since $\alpha+\beta > 1$, $\nabla V(x^*) = \mathbf{0}$ holds. For the second order condition, by (4.66)*, we have*

$$\nabla^2 L_\rho(y; x^*, v_1(x^*))|_{y=x^*} = \mathcal{H}(x^*; x^*) \succeq \mathbf{0}.$$

From the proof of theorem 4.6, we know that the eigenvalues of the Hessian matrix

$$\mathcal{H}(x^*; x^*) = \nabla^2 L_\rho(y; x^*, \mathbf{v}_1(x^*))|_{y=x^*}$$

is given by

$$\{(1-\alpha-\beta)\lambda_1(x^*), \lambda_2(x^*), \cdots, \lambda_d(x^*)\}.$$

Then we have that

$$\nabla^2 L_\rho(y; x^*, v_1(x^*))|_{y=x} \succeq \mathbf{0}$$

is equivalent to $\lambda_1(x^*) \le 0 \le \lambda_2(x^*) \le \cdots \le \lambda_d(x^*)$. By **Assumption** *2d, we know that x^* is non-degenerate with non-zero eigenvalues, thus*

$$\lambda_1(x^*) < 0 < \lambda_2(x^*) \le \cdots \le \lambda_d(x^*).$$

Together with $\nabla V(x^*) = \mathbf{0}$, we conclude that x^* is an index-1 saddle point of the potential function $V(\cdot)$. The proof of theorem 4.5 is now completed.